Stress-assisted (γ→α') and strain-induced (γ→ε→α') phase transformation kinetics laws implemented in a crystal plasticity model for predicting strain path sensitive deformation of austenitic steels

Zhangxi Feng, Milovan Zecevic, Marko Knezevic*

Department of Mechanical Engineering, University of New Hampshire, Durham, NH 03824, USA

Abstract

This paper formulates stress-assisted and strain-induced austenite to martensite transformation kinetics laws within a crystal plasticity framework to enable modeling of strain path sensitive elasto-plastic deformation of austenitic steels taking into account the evolution of crystallographic texture and the directionality of deformation mechanisms in the constituent phases. Consistent with experimental observations for mechanically induced martensitic transformation, the stress-assisted transformation is modeled as direct from γ-austenite to α'-martensite, while the strain-induced transformation is modeled as indirect through an intermediate ε-martensite phase, which subsequently transforms to α'-martensite. While the stress-assisted transformation law is conceived based on an energy criterion, the strain-induced transformation law relies on the local stress state sensitive motion of partial dislocations forming shear bands of ε-martensite phase, which after intersecting with other shear bands give rise to α'-martensite. The kinetic models are implemented in the elasto-plastic self-consistent polycrystal plasticity model to facilitate modeling of strain path and crystallographic texture dependence of martensitic transformation, while predicting deformation behavior of metastable austenitic steels. Due to its morphology, the ε-martensite is modeled using a flat ellipsoid approximation, which is a new numerical feature in the model. Simple tension, simple compression, and simple shear data of an austenitic steel have been used to calibrate and to illustrate predictive characteristics of the overall implementation. In doing so, stress-strain response, texture, and phase fractions of γ-austenite, intermediate ε-martensite, and α'-martensite are all calculated, while fully accounting for the crystallography of the transformation mechanisms. It is demonstrated that the appropriate modeling of phase fractions and crystallography facilitates predicting the experimentally measured data. The implementation and insights from these predictions are presented and discussed in this paper.

Keywords: A Phase transformation; A Microstructures; B Elastic-plastic material; B Crystal plasticity; C Numerical algorithms

---

*Corresponding author at: Department of Mechanical Engineering, University of New Hampshire, 33 Academic Way, Kingsbury Hall, W119, Durham, New Hampshire 03824, USA. Tel.: +1 603 862 5179; Fax: +1 603 862 1865; *E-mail address*: marko.knezevic@unh.edu

1. Introduction

Improved strength, work hardening rate, and formability of steels can be achieved by optimizing fraction and distribution of constituent phases, as well as grain size and crystal lattice orientation distributions per phase, and also by controlling the transformation-induced plasticity phenomena (Cantara et al., 2019; Olson and Cohen, 1972, 1975; Polatidis et al., 2018; Poulin et al., 2020a; Poulin et al., 2019; Poulin et al., 2020b; Talonen and Hänninen, 2007). Steels comprised of *γ*-austenite phase (face-centered cubic structure, FCC) either fully or in part can transform into *α'*-martensite (body-centered tetragonal structure, bct, which is usually approximated as body-centered cubic, BCC) upon deformation. The transformation contributes to the plastic flow and improves hardening behavior and formability of the material. The microstructural optimization of steels exhibiting transformation plasticity can be accelerated by the development of reliable material models sensitive to mechanically induced martensitic transformation. These models would facilitate better understanding of underlying phenomena and enable the prediction of mechanical response and microstructure evolution. The present work is concerned with formulating mechanically induced martensitic transformation kinetics laws within a crystal plasticity framework to enable simulating strain path sensitive elasto-plastic deformation of steels taking into account the evolution of crystallographic texture and the directionality of deformation mechanisms acting at grain level in the constituent phases.

During mechanical straining of steels containing metastable *γ*-austenite, nucleation sites for *α'*-martensite have been observed to be intersections of shear bands (Olson and Cohen, 1972, 1975; Polatidis et al., 2018; Talonen and Hänninen, 2007) and deformation twins (Das et al., 2016; Talonen and Hänninen, 2007). The martensite forming at these structural defects accommodating the plasticity is referred to as strain-induced (Haidemenopoulos et al., 2014; Olson and Azrin, 1978; Olson and Cohen, 1975; Yukio, 1987). The strain-induced martensite forms in the slip bands of the austenite as sheaves of fine parallel laths strung out on the $\{111\}_\gamma$ planes of the *γ*-austenite phase. In contrast, mechanically induced martensitic transformation can initiate from existing martensite formed either during cooling or mechanically (Tian et al., 2017). Transformation at such sites is referred to as stress-assisted (Olson, 2002; Olson and Cohen, 1972). The mechanically induced martensite sites are more effective for steels with lower stacking fault energy (SFE) (Tian et al., 2017). Together, a martensite transformation that occurs either via the stress-assisted or strain-induced mechanism is referred to as a mechanically induced martensite transformation (Marketz and Fischer, 1994). When both stress-assisted and strain-induced martensites form under deformation, it is observed that the strain-induced martensite forms first (Snell et al., 1977). However, the stress-assisted transformation can occur before yielding, while the strain-induced cannot (Olson and Cohen, 1982). Generally, the martensite formed during deformation is finer and less regular than the unstressed martensite formed during cooling (Snell et al., 1977).

Structural defects introduced by plastic deformation facilitating strain-induced α'-martensite nucleation are primarily intersections of slip bands formed by dissociation of perfect dislocation to partials (Olson and Cohen, 1972, 1975). If dislocations are at every 2nd $\{111\}_\gamma$ plane in austenite, the slip band has hexagonal close-packed (HCP) structure. This structure is ε-martensite phase. The HCP ε-martensite phase usually undergoes further transformation under continuous mechanical straining to the α'-martensite phase but can exist as a metastable phase depending on the conditions like strain level, temperature and

alloy chemistry. However, if dislocations are at every $\{111\}_\gamma$ plane in austenite, the band has the FCC structure and the twin orientation relationship with the parent grain. Formation of HCP or FCC within a slip band depends on the stacking fault energy. If stacking fault energy is low, formation of ε-martensite is preferred, while if the stacking fault energy is high, formation of twins is more prominent. The strain-induced transformation is strongly affected by crystal orientation (Burgers and Klostermann, 1965; Goodchild et al., 1970; Lagneborgj, 1964; Petit et al., 2007; Polatidis et al., 2018; Zecevic et al., 2019). Grains with $\langle 011 \rangle$ and $\langle 111 \rangle$ parallel to tension form slip bands of ε-martensite during deformation. In contrast, grains with $\langle 001 \rangle$ parallel to tension direction do not form slip bands (Goodchild et al., 1970) since partial dislocations do not have driving force to form wide stacking faults (Zecevic et al., 2019). Therefore, deformed microstructure of $\langle 011 \rangle$ and $\langle 111 \rangle$ grains consist of planar arrays of dislocations, while $\langle 001 \rangle$ grains developed cellular microstructure.

Due to the strain energy dominated nature of the stress-assisted martensite kinetics starting from available heterogeneous sites under deformation (Bhattacharyya and Weng, 1994), the transformation rates are intrinsically sensitive to the stress state caused by imposed boundary conditions as well as local stresses caused by adjacent transformations. The stress field that arises from a transformation interacts with the applied stress field in a way that may reduce or increase the change in free energy caused by the martensite transformation. If the shape change caused by transformation into a given variant out of 24 possible variants of martensite is compatible with the existing stress field then this variant forms and is said to be assisted by the given stress state. The volume fraction of transforming martensite vs plastic strain as a consequence of stress driven transformation shows linear behavior (Olson and Azrin, 1978).

Temperature, strain path, strain rate, crystallographic texture, and chemical composition are deformation conditions and microstructural features known to affect the rate of the martensitic transformation (Beese and Mohr, 2011; Han et al., 2004; Hecker et al., 1982; Iwamoto et al., 1998; Kim et al., 2015; Lebedev and Kosarchuk, 2000; Miller and McDowell, 1996; Shen et al., 2012; Talyan et al., 1998). The effects of chemical composition and temperature are linked with the SFE driving the stacking fault width (SFW) when a perfect dislocation dissociates into Shockley partials in FCC materials (Olson and Cohen, 1976; Talonen and Hänninen, 2007). Under the influence of external stress, the SFW increases resulting in the formation of a shear band.

The evolution of the volume fraction of α'-martensite during strain-induced transformation is typically a function of sigmoidal shape with respect to the plastic strain. Most of kinetic models for the strain-induced transformation present in the literature assume such functions for the evolution of α'-martensite volume fraction in terms of plastic strain (Olson and Cohen, 1975; Santacreu et al., 2006). Such observations formed based for the classical Olson-Cohen kinetics model (Olson and Cohen, 1975). Although empirical in nature, this model has been advanced in a number of studies to include variables characterizing the stress state like stress triaxiality (Haidemenopoulos et al., 2014; Santacreu et al., 2006; Stringfellow et al., 1992) and the Lode angle parameter (Beese and Mohr, 2011; Kim et al., 2015; Lebedev and Kosarchuk, 2000; Mansourinejad and Ketabchi, 2017). The addition of these variable makes the evolution of martensite using the extended Olson-Cohen kinetics model sensitive to strain paths. However, the strain path taken into account through the stress state parameters neglects the physics pertaining to the loading direction influencing the SFW (Copley and Kear, 1968) and shear bands (Byun,

2003; Martin et al., 2015; McCabe et al., 2014; Talonen and Hänninen, 2007; Ullrich et al., 2016). Diffraction experiments have shown that the suppression or facilitation of the martensitic transformation during plastic deformation stems from the changes in the SFW and the different resolved shear stresses imparted to the leading and trailing partial dislocations (Polatidis et al., 2018). More recently, crystallographic texture evolution has been incorporated into models for the martensitic transformation. To this end, the classical Olson-Cohen kinetic model has been incorporated into the visco-plastic self-consistent (VPSC) crystal plasticity model (Wang et al., 2016). The coupled model accounts for the role of crystal lattice orientation and anisotropy on plastic strain at the single crystal level in a polycrystal influencing the grain level martensite evolution. However, the underlying assumption in this model was that the martensite evolution per grain is purely a function of the plastic strain. As a result, any two grains with similar plastic strain evolution will have similar martensite fraction although their stress state may be different. While successful for uniaxial simulation cases, the implementation is not capable of predicting the strain path sensitivity of martensitic transformation. To relax the issue, another crystallographicaly extended Olson-Cohen kinetic model has been proposed and implemented in an elasto-plastic self-consistent (EPSC) crystal plasticity model (Zecevic et al., 2019). In this mode, the resolved shear stress on a slip plane in the direction perpendicular to the Burgers vector governs SFW and thus the local nucleation kinetics for shear band formation is sensitive to the local stress state. The model successfully interpreted and predicted the mechanical response, texture, and phase fractions for several austenitic steels subjected to simple tension (ST), simple compression (SC), plain strain tension, equibiaxial tension, and torsion.

The objective of this paper is to develop physically based kinetics models for both stress-assisted and strain-induced γ-austenite to α'-martensite transformation sensitive to strain path. The proposed model for the strain-induced transformation is not another extension of the empirical Olson-Cohen model but a more physical formulation involving partial dislocations. The strain-induced transformation model conceived here treats phase transformation physically as an additional deformation mode, while the stress-assisted transformation model relies on an energy criterion. Consistent with experimental observations, the kinetics model for the strain-induced transformation is first transforming γ-austenite to an intermediate ε-martensite phase in shear bands driven by local stress state sensitive motion of partial dislocations and subsequently transforming the ε-martensite phase to α'-martensite after shear bands intersect. In contrast, the stress-assisted transformation is direct from γ-austenite to α'-martensite kinetically driven by an energy criterion. Thus, crystallographic, kinetic, and thermodynamic aspects of the martensite transformation are captured by these laws. Since local crystal orientation has a strong influence on the active transformation mechanisms, the laws are implemented in EPSC, which was originally developed in (Turner and Tomé, 1994) and advanced in a number of studies (Barrett and Knezevic, 2019; Neil et al., 2010; Zecevic et al., 2017; Zecevic and Knezevic, 2015; Zecevic and Knezevic, 2017, 2018; Zecevic et al., 2015a; Zecevic et al., 2016b). The overall implementation facilitates modeling of strain path and crystallographic texture dependence of martensitic transformation, while predicting deformation behavior of metastable austenitic steels. ST, SC, and simple shear data of an austenitic steel have been used to calibrate and to illustrate predictive characteristics of the overall implementation. In doing so, stress-strain response, phase fractions of γ-austenite, intermediate ε-martensite, and α'-

martensite, and texture are all calculated, while fully accounting for the crystallography of the transformation mechanisms.

2. Modeling framework

This section presents kinetics models for mechanically induced martensitic transformation within a crystallography-based modeling framework of EPSC. The section begins with a summary of EPSC and then describes the stress-assisted and strain-induced transformation formulations. The formulations are physically based and do not assume functions for the evolution of α'-martensite fraction.

2.1 EPSC crystallographic platform for integrating phase transformation kinetic models

Notations with "·" representing a dot product and "⊗" representing a tensor product will be used in the description that follows. The original description of the EPSC model can be found in (Turner and Tomé, 1994). The model has been advanced since the original publication in a number of studies (Ghorbanpour et al., 2020; Ghorbanpour et al., 2017; Lentz et al., 2015a; Lentz et al., 2015b; Risse et al., 2017; Zecevic and Knezevic, 2019; Zecevic et al., 2015a; Zecevic et al., 2019). The particular version advanced here is from (Zecevic et al., 2019), where the martensitic phase transformation of several austenitic steels was modeled based on an extended Olson-Cohen kinetics model. The constitutive relation is:

$$\widehat{\boldsymbol{\sigma}}^c = \mathbf{C}^c\left(\dot{\boldsymbol{\varepsilon}}^c - \dot{\boldsymbol{\varepsilon}}^{pl,c} - \dot{\boldsymbol{\varepsilon}}^{pt,c}\right) - \boldsymbol{\sigma}^c tr(\dot{\boldsymbol{\varepsilon}}^c). \tag{1}$$

In Eq. (1), $\dot{\boldsymbol{\varepsilon}}^{pt,c}$ is the phase transformation rate of strain, $\widehat{\boldsymbol{\sigma}}^c$ is the Jaumann rate of stress, $\mathbf{C}^c$ is the elastic stiffness, $\dot{\boldsymbol{\varepsilon}}^c$ is the total rate of strain, and $\dot{\boldsymbol{\varepsilon}}^{pl,c}$ is the plastic rate of strain. As is evident, the total rate of strain includes the elastic, plastic and phase transformation contributions. The phase transformation rate of strain can further consist of strain-induced ($\dot{\boldsymbol{\varepsilon}}^{pt,\varepsilon,c}$) or stress-assisted ($\dot{\boldsymbol{\varepsilon}}^{pt,\sigma,c}$) portions, i.e. $\dot{\boldsymbol{\varepsilon}}^{pt,c} = \dot{\boldsymbol{\varepsilon}}^{pt,\varepsilon,c} + \dot{\boldsymbol{\varepsilon}}^{pt,\sigma,c}$. In our implementation, an austenite grain can form either stress-assisted or strain-induced martensite. If an austenite grain forms stress-assisted martensite first, it can also form strain-induced martensite while the progression of the stress-assisted transformation is terminated. The plastic strain is calculated using $\dot{\boldsymbol{\varepsilon}}^{pl,c} = \sum_s \mathbf{m}^s \dot{\gamma}^s$ with $\mathbf{m}^s = \frac{1}{2}(\mathbf{b}^s \otimes \mathbf{n}^s + \mathbf{n}^s \otimes \mathbf{b}^s)$, where $\mathbf{b}^s$ is the unit slip system Burgers vector and $\mathbf{n}^s$ is the slip system unit normal vector. $\dot{\gamma}^s$ is a shear rate on the slip system, *s*. A slip systems activates upon $\boldsymbol{\sigma}^c \cdot \mathbf{m}^s = \tau_c^s$ and $\widehat{\boldsymbol{\sigma}}^c \cdot \mathbf{m}^s = \dot{\tau}_c^s$ conditions are fulfilled. Here, τ_c^s is the slip resistance of a slip system *s* (appendix A). The single crystal constitutive relation is conveniently expressed as:

$$\widehat{\boldsymbol{\sigma}}^c = \mathbf{L}^c(\dot{\boldsymbol{\varepsilon}}^c - \dot{\boldsymbol{\varepsilon}}^{pt,c}) = \dot{\boldsymbol{\sigma}}^c + \boldsymbol{\sigma}^c\mathbf{W}^c - \mathbf{W}^c\boldsymbol{\sigma}^c. \tag{2}$$

In Eq. (2), $\mathbf{L}^c$ is the instantaneous elasto-plastic stiffness, $\mathbf{W}^c$ is grain spin tensor, and $\boldsymbol{\sigma}^c$ is Cauchy crystal level stress. $\mathbf{L}^c$ is derived using a selected hardening law and the crystal constitutive law using

$$\mathbf{L}^c = \mathbf{C}^c - \mathbf{C}^c \sum_s \mathbf{m}^s \otimes \left(\sum_{s'}\left(X^{ss'}\right)^{-1}\mathbf{m}^{s'}\left(\mathbf{C}^c - \boldsymbol{\sigma}^c \otimes \mathbf{i}\right)\right) - \boldsymbol{\sigma}^c \otimes \mathbf{i} \tag{3}$$

with $X^{ss'} = h^{ss'} + \mathbf{C}^c \cdot \mathbf{m}^s \otimes \mathbf{m}^{s'}$, $h^{ss'} = \frac{\partial \tau_c^s}{\partial \gamma^{s'}}$, and $\mathbf{i}$ is the second rank identity matrix. Similarly, the polycrystal constitutive relation is:

$$\widehat{\boldsymbol{\sigma}} = \mathbf{L}(\dot{\boldsymbol{\varepsilon}} - \dot{\boldsymbol{\varepsilon}}^{pt}) = \dot{\boldsymbol{\sigma}} - \langle \mathbf{W}^c \boldsymbol{\sigma}^c \rangle + \langle \boldsymbol{\sigma}^c \mathbf{W}^c \rangle. \quad (4)$$

Here, $\widehat{\boldsymbol{\sigma}}$ is the Jaumann stress rate, $\dot{\boldsymbol{\varepsilon}}$ is the total rate of strain, and $\dot{\boldsymbol{\varepsilon}}^{pt}$ is the phase transformation rate of strain of the polycrystal, while $\mathbf{L}$ is the instantaneous elasto-plastic stiffness of the homogenized polycrystal. $\langle \quad \rangle$ indicates the volume average. The phase transformation rate of strain at the polycrystal level can further consist of the strain-induced and stress-assisted portions. $\mathbf{L}$ and $\dot{\boldsymbol{\varepsilon}}^{pt}$ are unknown and are evaluated using the standard self-consistent homogenization scheme (Masson et al., 2000; Zecevic and Knezevic, 2018). To this end, the difference between a crystal stress rate and the stress rate of the polycrystal is proportional to the difference in strain rates using the interaction tensor, $\mathbf{L}^*$:

$$\widehat{\boldsymbol{\sigma}}^c - \widehat{\boldsymbol{\sigma}} = -\mathbf{L}^*(\dot{\boldsymbol{\varepsilon}}^c - \dot{\boldsymbol{\varepsilon}}). \quad (5)$$

The tensor $\mathbf{L}^*$ is defined in terms of the symmetric Eshelby tensor, $\mathbf{S}^c$, as: $\mathbf{L}^* = \mathbf{L}\left(\mathbf{S}^{c^{-1}} - \mathbf{I}\right)$. Combining Eqs. (2), (4) and (5) results with:

$$\mathbf{L}^c(\dot{\boldsymbol{\varepsilon}}^c - \dot{\boldsymbol{\varepsilon}}^{pt,c}) - \mathbf{L}(\dot{\boldsymbol{\varepsilon}} - \dot{\boldsymbol{\varepsilon}}^{pt}) = -\mathbf{L}^*(\dot{\boldsymbol{\varepsilon}}^c - \dot{\boldsymbol{\varepsilon}}). \quad (6)$$

From Eq. (6), the crystal level rate of strain in terms of the unknown reference rate of strain is (Lebensohn et al., 1996):

$$\dot{\boldsymbol{\varepsilon}}^c = \mathbf{A}^c \dot{\boldsymbol{\varepsilon}}^{ref} + \mathbf{a}^c, \quad (7)$$

with:

$$\mathbf{A}^c = (\mathbf{L}^c + \mathbf{L}^*)^{-1}(\mathbf{L} + \mathbf{L}^*), \quad (8)$$

$$\mathbf{a}^c = (\mathbf{L}^c + \mathbf{L}^*)^{-1}(\mathbf{L}^c \dot{\boldsymbol{\varepsilon}}^{pt,c} - \mathbf{L}\dot{\boldsymbol{\varepsilon}}^{pt}). \quad (9)$$

Here, $\dot{\boldsymbol{\varepsilon}}^{ref}$ is the reference rate of strain. Equating the volume average of the crystal level rates of strain to the rate of strain of the polycrystal results with an equation for $\dot{\boldsymbol{\varepsilon}}^{ref}$ as:

$$\dot{\boldsymbol{\varepsilon}}^{ref} = \langle \mathbf{A}^c \rangle^{-1} \dot{\boldsymbol{\varepsilon}} - \langle \mathbf{A}^c \rangle^{-1} \langle \mathbf{a}^c \rangle. \quad (10)$$

Since the volume average of the crystal level stress rates is equal to that of the polycrystal, the Jaumann stress rate is:

$$\widehat{\boldsymbol{\sigma}} = \langle \mathbf{L}^c \mathbf{A}^c \rangle \langle \mathbf{A}^c \rangle^{-1} \dot{\boldsymbol{\varepsilon}} - \langle \mathbf{L}^c \mathbf{A}^c \rangle \langle \mathbf{A}^c \rangle^{-1} \langle \mathbf{a}^c \rangle + \langle \mathbf{L}^c (\mathbf{a}^c - \dot{\boldsymbol{\varepsilon}}^{pt,c}) \rangle \quad (11)$$

The instantaneous elasto-plastic stiffness and the phase transformation strain rate are obtained by comparing Eqs. (4) and (11):

$$\mathbf{L} = \langle \mathbf{L}^c \mathbf{A}^c \rangle \langle \mathbf{A}^c \rangle^{-1}, \quad (12)$$

$$\dot{\boldsymbol{\varepsilon}}^{pt} = \langle \mathbf{a}^c \rangle - \mathbf{L}^{-1} \langle \mathbf{L}^c (\mathbf{a}^c - \dot{\boldsymbol{\varepsilon}}^{pt,c}) \rangle. \quad (13)$$

Finally, for texture evolution, the rate of spin of a crystal *c* is:

$$\mathbf{W}^c = \mathbf{W}^{c,app} - \mathbf{W}^{pl,c}, \tag{14}$$

where $\mathbf{W}^{c,app}$ is an applied spin and $\mathbf{W}^{pl,c}$ is a plastic spin. The applied spin consists of an overall applied macroscopic spin, $\mathbf{W}$, and a spin originating from the antisymmetric Eshelby tensor for crystal *c*, $\mathbf{\Pi}^c$. Using the Eshelby solution for a grain inhomogeneity inside the effective medium under a given boundary conditions, the spin is $\mathbf{\Pi}^c = \mathbf{P}^c(\mathbf{S}^c)^{-1}(\dot{\boldsymbol{\varepsilon}}^c - \dot{\boldsymbol{\varepsilon}})$. Here, $\mathbf{P}^c$ is the antisymmetric Eshelby tensor. The plastic spin is $\mathbf{W}^{pl,c} = \sum_s \dot{\gamma}^s \mathbf{q}^s$ with $\mathbf{q}^s = \frac{\mathbf{1}}{\mathbf{2}}(\mathbf{b}^s \otimes \mathbf{n}^s - \mathbf{n}^s \otimes \mathbf{b}^s)$.

2.2 Kinetics model for stress-assisted martensitic transformation under mechanical load

The formation of stress-assisted martensite is the result of the interaction of the applied stress with the transformation strain to give an energetic contribution to the driving force for the martensite transformation (Maxwell et al., 1974). The transformation occurs when the summation of chemical driving force and mechanical driving force reaches a critical value. The mechanical driving force is defined as:

$$U = \boldsymbol{\sigma}^c \cdot \boldsymbol{\varepsilon}^{pt,\sigma}\,, \tag{15}$$

where $\boldsymbol{\sigma}^c$ is the stress in an austenite grain and $\boldsymbol{\varepsilon}^{pt,\sigma}$ is the phase transformation strain. Ignoring the interfacial energy and the boundary misfit strain energy, the stress-assisted transformation occurs once the mechanical driving force is fulfilling the relation:

$$U = U_c\,, \tag{16}$$

where U_c is the critical force (Levitas et al., 1998). In our self-consistent formulation, a crystal is an inclusion surrounded by matrix having homogenous effective properties. Given an applied deformation, grain level as well as the overall stress-strain values are calculated using EPSC. When Eq. (16) is satisfied in any inclusion grain, the transformation starts. It is assumed that every inclusion has a pre-existing site created during cooling or a site from a prior mechanically induced transformation for subsequent stress-assisted transformation. Driving force or potency for transformation at each site is a uniform grain stress, which is used to test the condition, Eq. (16). U_c can be interpreted as an average critical driving force over all nucleation sites. The eigenstrain i.e. stress free change of shape and volume, is added to the inclusion corresponding to the phase transformation strain and volume fraction of the martensite (Eqs. (1) and (2)). The increment in the phase transformation strain assigned to the austenite grain, $\Delta\boldsymbol{\varepsilon}^{pt,\sigma,c} = \dot{\boldsymbol{\varepsilon}}^{pt,\sigma,c}\Delta t$, is calculated using:

$$\Delta\boldsymbol{\varepsilon}^{pt,\sigma,c} = \Delta f^{\alpha,\sigma}\boldsymbol{\varepsilon}^{pt,\sigma} \tag{17}$$

where $\Delta f^{\alpha,\sigma}$ is the increment in the volume fraction of martensite relative to the austenite grain volume and $\boldsymbol{\varepsilon}^{pt,\sigma}$ is the phase transformation strain of the transforming volume. $\Delta f^{\alpha,\sigma}$ is calculated by satisfying the following condition:

$$\Delta U = \Delta\boldsymbol{\sigma}^c \cdot \boldsymbol{\varepsilon}^{pt,\sigma} = 0\,. \tag{18}$$

The equation is stating that the total applied driving force cannot be larger than critical driving force, otherwise further transformation would occur until the matrix constraining the grain induces the stress necessary to stop the transformation. From Eq. (18), we can calculate increment in martensite volume fraction as:

$$\Delta f^{\alpha,\sigma} = \frac{\boldsymbol{\varepsilon}^{pt,\sigma} \cdot (\mathbf{L}^c \Delta \boldsymbol{\varepsilon}^c)}{\boldsymbol{\varepsilon}^{pt,\sigma} \cdot (\mathbf{L}^c \boldsymbol{\varepsilon}^{pt,\sigma})}. \tag{19}$$

The volume fraction evolution is calculated for every of 24 possible α'-martensite variants fulfilling the condition of Eq. (18). From Eq. (19), we get that $\Delta f^{\alpha,\sigma}$ is approximately linearly proportional to the strain, $\Delta \boldsymbol{\varepsilon}^c$, as observed in (Olson and Azrin, 1978). For simplicity, in our implementation only the most active variant is re-oriented into a new α'-martensite grain as soon as the volume fraction of the variant reaches a threshold value, $f_{\alpha'}^{cr} = 0.01$. The initial stress and strain is the new grain are set equal to the austenite parent grain. Details pertaining to the crystal lattice orientation of the new grain along with the variant selection and phase transformation strain are provided in appendix B.

2.3 Kinetics model for strain-induced martensitic transformation under mechanical load

As the formation of α' phase in the strain-induced manner involves an intermediate ε phase, we first describe $\gamma \rightarrow \varepsilon$ and then $\varepsilon \rightarrow \alpha'$.

2.3.1 $\gamma \rightarrow \varepsilon$

The formation of slip bands is a prerequisite for strain-induced transformation. Slip bands occur once the local stress causes the separation between partials to increase and span the whole grain, thereby increasing the area of stacking fault (SF) between partials. Slip bands usually include multiple dislocations on nearby $\{111\}_\gamma$ planes. These partial dislocations on neighboring $\{111\}_\gamma$ planes can be treated as superdislocations which are boundaries of a thick fault (Olson and Cohen, 1976). The term slip band is used for thick faults that have expanded under the action of applied stress to span the whole grain as very thin bands. Although spanning the entire inclusion, the thickness of a slip band is small requiring a flat ellipsoid formulation in EPSC, as will be described shortly. Following the derivation presented in (Zecevic et al., 2019), the separation between superdislocations is:

$$d = cN^2 \,/\, \left[2\gamma_N - Nb_p \left(\left(\hat{\mathbf{b}}_l - \hat{\mathbf{b}}_r \right) \boldsymbol{\sigma}^c \right) \cdot \hat{\mathbf{n}} \right] \tag{20}$$

where N is the number of intrinsic SF in the thick fault, γ_N is the fault energy, b_p is magnitude of the Burgers vector of partial dislocation, $\hat{\mathbf{b}}_l$ is a unit vector in the direction of left partial, $\hat{\mathbf{b}}_r$ is a unit vector in the direction of right partial, $\boldsymbol{\sigma}^c$ is the stress in the crystal, c, and $\hat{\mathbf{n}}$ is the glide plane normal unit vector. The thick fault can have either FCC or HCP structure, depending on the ratio between the intrinsic SFE and the surface energy of the fault. The surface energy is the free energy per unit area of the austenite/martensite interface (Olson and Cohen, 1976). In this study we will focus on the case when the thick fault has HCP structure, meaning that the intrinsic SFE is lower than the surface energy of the fault. The formed HCP structure inside the fault is the ε-martensite.

If under the applied stress, $\boldsymbol{\sigma}^c$, denominator in Eq. (20) tends to zero, the separation of superdislocations, d, will tend to infinity. Therefore, the following condition can be used to test whether a slip band is present on a given slip system and in the grain under stress $\boldsymbol{\sigma}^c$:

$$2\gamma_N - Nb_p\left(\left(\hat{\mathbf{b}}_l - \hat{\mathbf{b}}_r\right)\boldsymbol{\sigma}^c\right)\cdot\hat{\mathbf{n}} \leq 0. \tag{21}$$

If a slip band is formed by one active slip system in a given grain, all other active slip systems within the grain are assumed to form slip bands. The formation of only one slip band will initiate the creation of slip bands on intersecting slip systems, since the slip band allows only leading partials to pass. As partial dislocations are moving on the intersecting slip systems, a leading partial enters the given slip band and glides on a pyramidal slip system in the band of ε-martensite contributing to the subsequent formation of α'-martensite within the band, which will be described in the next section. The trailing partial stays pinned at the shear band. The leading partial can exit the band and continue moving, creating a new shear band since the trailing partial is left behind pinned at the boundary of the sheared band. In summary, once Eq. (21) is fulfilled for one active slip system in the grain, bands of all active slip systems in the grain form ε-martensite, while the intersections form α'-martensite.

The ε-martensite volume fraction increment is proportional to shear strain increment:

$$\Delta f^{s,\varepsilon} = \frac{\Delta\gamma^{s,p}}{s^{\varepsilon}}, \tag{22}$$

where $\Delta f^{s,\varepsilon}$ is the ε-martensite volume fraction increment, $\Delta\gamma^{s,p}$ is the shear strain increment in the direction $\langle 1\bar{1}\bar{2}\rangle_\gamma$ on the $\{1\bar{1}1\}_\gamma$ plane and s^{ε} is the characteristic shear related to the austenite to ε-martensite transformation. The shear increment in the direction $\langle 110\rangle_\gamma$ is $\Delta\gamma^{s}$. Thus, $\Delta\gamma^{s,p}$ can be calculated using:

$$\Delta\gamma^{s,p} = \frac{\Delta\gamma^{s}}{\cos 30^\circ} = \frac{2}{\sqrt{3}}\Delta\gamma^{s}, \tag{23}$$

where, $\cos 30^\circ$ is the dot product between $\langle 1\bar{1}\bar{2}\rangle_\gamma$ and $\langle 110\rangle_\gamma$. The remaining shear strain produced by leading partial is in direction $\left(\hat{\mathbf{b}}_l - \hat{\mathbf{b}}_r\right)$ for $\frac{1}{2}\Delta\gamma^{s,p}$. This shear strain is assigned as eigenstrain to parent austenite grain. The characteristic shear is:

$$s^{\varepsilon} = \frac{s^{tw}}{2} = \frac{1}{2\sqrt{2}}, \tag{24}$$

where s^{tw} is the characteristic twinning shear (Christian and Mahajan, 1995). The relationship is derived from the fact that twins are produced by passage of partial dislocations on every $\{111\}_\gamma$ plane, while ε-martensite is produced by passage of partial dislocations on every 2nd $\{111\}_\gamma$ plane. Therefore, if the volume of twin and the ε-martensite is the same, the shear strain accommodated by twin is two times larger than the shear strain accommodated by ε-martensite.

The volume fraction of ε-martensite bands in a given grain is driven by the shear strain increments (Eq. (22)). A new grain representing ε-martensite is introduced once the volume fraction of ε-martensite reaches a threshold value, $f_{cr}^{\varepsilon} = 0.01$ per variant. In our implementation, multiple ε -martensite

grains/variants are allowed to form. However, only one with the highest propensity to be wide will be selected for the re-orientation into an α'-martensite grain. An ε-martensite grain is contained within a slip band spanning over the whole grain but the thickness is small corresponding to its volume fraction. Since we use a self-consistent model we need to represent the new grain as an ellipsoidal inclusion in the matrix. Fitting an ellipsoid to the slip band results in an ellipsoid with two axis of similar length, $a_1 \approx a_2$, while the length of the third axis is several orders of magnitude lower, $a_3 \ll a_1, a_2$. Such ellipsoids are referred to as flat. Regular numeric integration of Green tensor, necessary to find the Eshelby tensor, will provide erroneous results. The issue can be resolved by using a flat ellipsoid approximation i.e letting $a_3 \to 0$ (Huang and Liu, 1998). Therefore, we use expressions from (Huang and Liu, 1998) to calculate the Eshelby tensor for flat ellipsoids that are representing the ε-martensite. The results of flat ellipsoid approximation are validated by using a regular definition of integrals in Eshelby tensor calculation and performing the numerical integration with the integral2 function in Matlab, which is able to handle highly oscillating integrand function accurately.

The initial stress and strain of the new grain are set equal to the austenite parent grain. The elastic spin of ε-martensite grains, used to evolve the crystal orientation, is enforced to be the same as the parent austenite grains. The crystal orientation of ε-martensite formed on a slip system defined with plane normal, $\mathbf{n}_\gamma = \{1\bar{1}1\}_\gamma$, and burgers vector of perfect dislocation, $\mathbf{b}_\gamma = \langle 110\rangle_\gamma$, is:

$$\mathbf{n}_\gamma \parallel \{000\bar{1}\}_\varepsilon \tag{25a}$$

$$\mathbf{b}_\gamma \parallel \langle 2\bar{1}\bar{1}0\rangle_\varepsilon \,. \tag{25b}$$

Given slip system plane normals and Burgers vectors of ε-martensite perfect dislocations, the orientations of multiple ε-martensite grains are determined using Eq. (25). It is already indicated that for simplicity of our implementation, only one of multiple ε-martensite grains possible to form in a given austenite grain will give the crystal orientation to a new α'-martensite grain. It is the ε-martensite band having the highest separation. As a result, one austenite grain is producing one α'-martensite grain, although multiple ε-martensite bands have formed in the austenite grain. The active deformation modes and corresponding slip resistance of ε-martensite are closely related to α'-martensite formation. Therefore, these aspects will be discussed after considering the α'-martensite transformation.

2.3.2 $\varepsilon \to \alpha'$

Transformation of FCC to BCC by means of two slip bands involves: *T*/2 shear, *T*/3 shear and a volume change (Bogers and Burgers, 1964; Olson and Cohen, 1972). In the description that follows, shear is a uniform deformation of a block of atoms, which is usually produced by either or both dislocations and shuffles. A shuffle is a translation of atomic planes, while a dislocation moves one half of the crystal for a Burger vector. Two mechanisms for the formation of α'-martensite from ε-martensite are distinguished: within ε-martensite bands at slip band intersections (Yang et al., 2014) and within ε -martensite bands but not at slip band intersections (Yang et al., 2015). Both mechanisms can be reduced to a combination of the *T*/2 and *T*/3 shears that produce BCC structure from the FCC structure containing ε-martensite bands, where *T* refers to the twinning shear. *T*/2 and *T*/3 shears refer to lattice deformation and structures produced by uniform shearing of FCC lattice. Thus, these shears are relative to the FCC structure. ε-

martensite can be converted to either *T*/2 or *T*/3 shear structures with appropriate atom shuffles and the introduction of dislocations. Thus, following the formation of shear bands with HCP structure and upon encountering of two of them, one of the bands spontaneously undergoes a shuffle to form a *T*/2 structure, while the other band introduces a *T*/3 shear over the intersecting region undergoing the transformation. It is not clear whether *T*/2 shear or *T*/3 shear happen first. The other shear producing α'-martensite (*T*/3 if *T*/2 happened first or *T*/2 if *T*/3 happened first) can be introduced by passing partial dislocations from surrounding austenite or it can initiate in the ε-martensite. The later refers to the mechanism of α'-martensite formation without slip band intersections but plastic deformation of ε by pyramidal slip. In both cases, with and without intersecting bands, certain amount of plastic strain is accommodated in the ε-martensite accompanied by the transformation to α'-martensite. Therefore, we relate the α'-martensite to the plastic deformation of ε-martensite without making a clear distinction between the partials that come from austenite and partials that are nucleated within ε-martensite.

We consider the case in which ε-martensite is converted to *T*/2 structure by shuffle on every 2nd $\{0001\}_\varepsilon$ plane in $\frac{a_\gamma}{12}\langle 1\bar{1}\bar{2}\rangle_\gamma$ (Bracke et al., 2007). By applying this shuffle, two $\{01\bar{1}1\}_\varepsilon$ planes become uniformly distorted $\{111\}_\gamma$ planes. The *T*/3 shear is then on $\{01\bar{1}1\}_\varepsilon$ planes (Yang et al., 2015). As is evident, the directions and planes are described in different structures, some intuitive in FCC and some in HCP. For example, $\{0001\}_\varepsilon$ is in the HCP structure because the translation/shuffle is applied to it. However, the Burgers direction of the partial dislocation ($\frac{a_\gamma}{12}\langle 1\bar{1}\bar{2}\rangle_\gamma$) is much more intuitive in FCC, as it has no special meaning when converted to the HCP structure. Figure 1a and b show appearance of one $\{01\bar{1}1\}_\varepsilon$ planes produced by applying two different shuffles in $\frac{a_\gamma}{12}\langle 1\bar{1}\bar{2}\rangle_\gamma$ on every 2nd $\{0001\}_\varepsilon$ plane. More elaborate description is given in appendix C. From Figure 1 it is seen that on every $\{01\bar{1}1\}_\varepsilon$ plane there are two directions for *T*/3 shear that will produce the BCC structure, depending on the *T*/2 shear direction (Bogers and Burgers, 1964; Bracke et al., 2007; Olson and Cohen, 1972). Specifically, there are two equally possible shuffles that produce two different distortions of one $\{01\bar{1}1\}_\varepsilon$ plane, shown in Fig. 1. For each distortion there is one *T*/3 shear that will produce the BCC structure. The angle between $\langle 0\bar{1}12\rangle_\varepsilon$ direction and *T*/3 shearing direction is $\approx 126°$, meaning that *T*/3 direction corresponds to $\approx \langle 5\bar{1}\bar{4}\bar{3}\rangle_\varepsilon$. It appears that partial dislocations that cause contraction of **c**-axis of ε-martensite form BCC, while partial dislocations causing extension of **c**-axis of ε-martensite do not form BCC. Hence, we restrict the shearing of ε-martensite on the $\{01\bar{1}1\}_\varepsilon$ planes in the $\langle 5\bar{1}\bar{4}\bar{3}\rangle_\varepsilon$ directions to those satisfying $\langle 5\bar{1}\bar{4}\bar{3}\rangle_\varepsilon \cdot [0001] < 0$. However, no such restriction has been reported in any experimental observations. To facilitate **c**-axis extension in ε-martensite and the fact that every intersection forms α-martensite, we assume that in case of partial dislocations causing the extension of **c**-axis, ε-martensite is converted to *T*/3 shear structure by the introduction of appropriate shuffles and *T*/6 shear (Yang et al., 2015). This is the case when the ε-martensite transforms to *T*/3 structure first. Then the missing shear is *T*/2. The necessary *T*/2 shear is formed by passing dislocations and appropriate shuffles over the *T*/3 structure to get α'-martensite. We model this situation by considering shearing of ε-martensite in the $\langle 0\bar{1}12\rangle_\varepsilon$ direction on the planes $\{01\bar{1}1\}_\varepsilon$, with the following restriction $\langle 0\bar{1}12\rangle_\varepsilon \cdot [0001] > 0$. The orientation relationship between austenite, ε-martensite and α'-martensite is (Bracke et al., 2007):

$$\{111\}_\gamma \parallel \{0001\}_\varepsilon \parallel \{110\}_{\alpha'} \quad (26a)$$

$\langle 110\rangle_\gamma \parallel \langle 2\bar{1}\bar{1}0\rangle_\varepsilon \parallel \langle 111\rangle_{\alpha'}$. (26b)

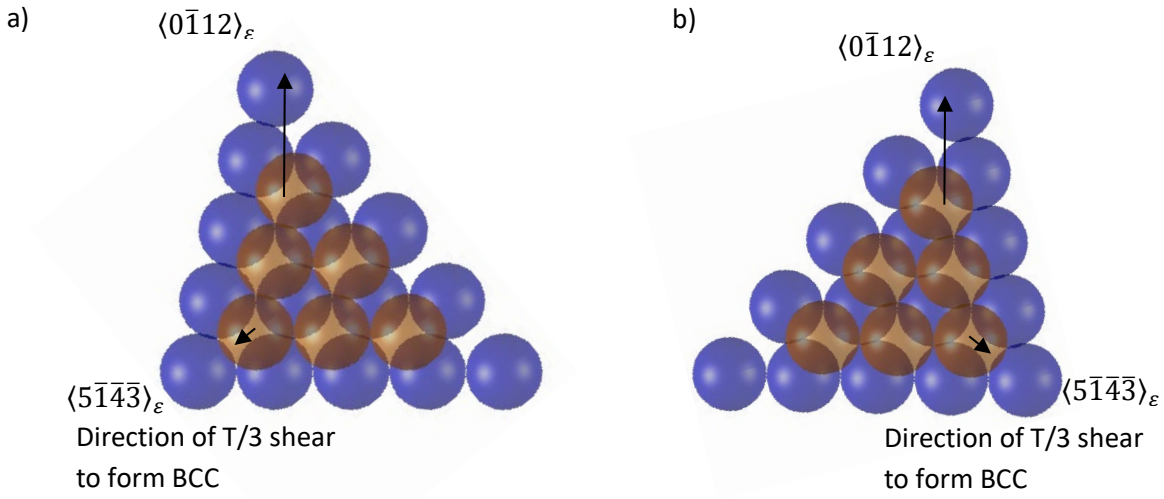

Figure 1. Schematic showing uniformly distorted $\{111\}_\gamma$ planes (or equivalently $\{01\bar{1}1\}_\varepsilon$ planes) after *T*/2 shear by two possible shuffles in $\frac{a_\gamma}{12}\langle 1\bar{1}\bar{2}\rangle_\gamma$ on every 2nd $\{111\}_\gamma$ (or equivalently $\{0001\}_\varepsilon$). Subsequent *T*/3 shear to get BCC structure is indicated in the figure. The views are along the normal to $\{111\}_\gamma$ planes that are distorted. Both blue and brown atoms make up the same distorted planes.

The description above was about the mechanism for the formation of the α'-martensite from the ε-martensite within the ε-martensite bands upon intersections with other slip bands. We now turn our attention to the mechanism of α' -martensite formation within ε-martensite bands but not at intersections with other slip bands. Here, we assume that ε-martensite plastically deforms by shearing on the planes $\{01\bar{1}1\}_\varepsilon$ in the directions $\langle 5\bar{1}\bar{4}\bar{3}\rangle_\varepsilon$ and $\langle 0\bar{1}12\rangle_\varepsilon$, with the restrictions $\langle 5\bar{1}\bar{4}\bar{3}\rangle_\varepsilon \cdot [0001] < 0$ and $\langle 0\bar{1}12\rangle_\varepsilon \cdot [0001] > 0$. In our implementation, these two directions on $\{01\bar{1}1\}_\varepsilon$ are provided as available slip systems for the ε-martensite phase (table 1). The shear is directional, meaning that it happens only in one sense.

Table 1. List of pyramidal slip systems in HCP phase.

n	b
$0\ 1\ \bar{1}\ 1$	$0\ \bar{1}\ 1\ 2$
$0\ 1\ \bar{1}\ 1$	$5\ \bar{1}\ \bar{4}\ \bar{3}$
$0\ 1\ \bar{1}\ 1$	$\bar{5}\ 4\ 1\ \bar{3}$
$1\ 0\ \bar{1}\ 1$	$\bar{1}\ 0\ 1\ 2$
$1\ 0\ \bar{1}\ 1$	$\bar{1}\ 5\ \bar{4}\ \bar{3}$

$1\ 0\ \bar{1}\ 1$	$4\ \bar{5}\ 1\ \bar{3}$
$1\ \bar{1}\ 0\ 1$	$\bar{1}\ 1\ 0\ 2$
$1\ \bar{1}\ 0\ 1$	$4\ 1\ \bar{5}\ \bar{3}$
$1\ \bar{1}\ 0\ 1$	$\bar{1}\ \bar{4}\ 5\ \bar{3}$
$0\ \bar{1}\ 1\ 1$	$0\ 1\ \bar{1}\ 2$
$0\ \bar{1}\ 1\ 1$	$5\ \bar{4}\ \bar{1}\ \bar{3}$
$0\ \bar{1}\ 1\ 1$	$\bar{5}\ 1\ 4\ \bar{3}$
$\bar{1}\ 0\ 1\ 1$	$1\ 0\ \bar{1}\ 2$
$\bar{1}\ 0\ 1\ 1$	$\bar{4}\ 5\ \bar{1}\ \bar{3}$
$\bar{1}\ 0\ 1\ 1$	$1\ \bar{5}\ 4\ \bar{3}$

As mentioned above, both mechanisms (with and without intersecting bands) are a combination of the *T*/2 and *T*/3 shears that produce BCC structure from the FCC structure containing ε-martensite bands. The increment in volume fraction of α'-martensite is related to the shear increments through the characteristic shear of transformation:

$$\Delta f^{s,\alpha'} = \frac{\Delta\gamma^s}{s^{\varepsilon\to\alpha'}}, \tag{27}$$

where $\Delta f^{\alpha'}$ is the increment in volume fraction of α'-martensite with respect to ε-martensite, $\Delta\gamma^s$ is the increment in shear strain on the planes $\{01\bar{1}1\}_\varepsilon$ in the directions $\langle 5\bar{1}\bar{4}\bar{3}\rangle_\varepsilon$ and $\langle 0\bar{1}12\rangle_\varepsilon$, with the two restrictions $\langle 5\bar{1}\bar{4}\bar{3}\rangle_\varepsilon \cdot [0001] < 0$ and $\langle 0\bar{1}12\rangle_\varepsilon \cdot [0001] > 0$, and $s^{\varepsilon\to\alpha'} = \frac{1}{3\sqrt{2}}$ is the characteristic shear of $\varepsilon \to \alpha'$ transformation. To calculate the total volume fraction of α'-martensite, for simplicity we sum α'-martensite volume fractions from all ε-martensite grains having the same parent austenite grain instead of modeling multiple α'-martensite child grains. Hence, we assign one volume fraction of α'-martensite to each austenite grain that is transforming. Once the volume fraction of α'-martensite reaches a critical value of, $f_{cr}^{\alpha'} = 0.01$, a new α'-martensite grain is introduced into the polycrystal. The parent ε-martensite band for re-orienting is the one exhibiting the highest separation, while selecting the *T*/3 slip system involves a search for the one active system within the parent austenite grain giving rise to the α'-martensite crystal orientation. Only a specific combination of *T*/2 shuffle followed by *T*/3 shear will give α'. If multiple slip systems satisfy the condition to give α', the one with the highest driving force is selected. More details on the orientation of the new grain and the phase transformation strain are given in appendix C. The calculated phase transformation strain is averaged over the austenite grain and assigned to: (1) austenite parent, (2) ε-martensite grains nucleated from austenite parent and (3) newly created α'-martensite grain. Thus, the eigenstrain is assigned to austenite grain and all its product phases i.e. ε and α'. In that process, it needs to be averaged over the volume of all the grains that nucleated from the original austenite grain, since EPSC only understands one value of a uniform average eigenstrain per grain (Zecevic et al., 2019). Figure 2 presents a schematic showing an austenite grain represented with a sphere before and after martensitic transformation.

The mechanical driving force for $\varepsilon \to \alpha'$ transformation reduces to:

$$U^s = \tau^s \frac{T}{3} + \boldsymbol{\sigma}^{hyd} \cdot \boldsymbol{\varepsilon}^{pt,\varepsilon}, \tag{28}$$

where τ^s is the shear stress in the direction of the *T*/3 shear in ε-martensite, $\boldsymbol{\sigma}^{hyd}$ is the hydrostatic stress and $\boldsymbol{\varepsilon}^{pt,\varepsilon}$ is the phase transformation strain related to the volume change (see appendix C, Eq. (C5)). In other words, τ^s is the resolved shear stress on $\{01\bar{1}1\}_\varepsilon$ in directions $\langle 5\bar{1}\bar{4}\bar{3}\rangle_\varepsilon$ and $\langle 0\bar{1}12\rangle_\varepsilon$, with the restrictions $\langle 5\bar{1}\bar{4}\bar{3}\rangle_\varepsilon \cdot [0001] < 0$ and $\langle 0\bar{1}12\rangle_\varepsilon \cdot [0001] > 0$. Note that for simplicity, we do not make a distinction between driving force for $\langle 5\bar{1}\bar{4}\bar{3}\rangle_\varepsilon$ and $\langle 0\bar{1}12\rangle_\varepsilon$ slip systems, even though according to the discussion above $\langle 5\bar{1}\bar{4}\bar{3}\rangle_\varepsilon$ is the direction for *T*/3 shear and $\langle 0\bar{1}12\rangle_\varepsilon$ is the direction of *T*/2 shear. The $\varepsilon \rightarrow \alpha'$ transformation occurs when the mechanical driving force reaches a critical value:

$$\tau^s \frac{T}{3} + \boldsymbol{\sigma}^{hyd} \cdot \boldsymbol{\varepsilon}^{pt,\varepsilon} = U_{cr} \,. \tag{29}$$

The critical U_{cr} mechanical driving force is the difference between the chemical driving force at which transformation occurs spontaneously and the chemical driving force at current temperature. It has a similar interpretation as U_c in Eq. (16). Since the $\varepsilon \rightarrow \alpha'$ transformation occurs by motion of partial dislocation averaging one on every three $\{01\bar{1}1\}_\varepsilon$ planes, we rewrite Eq. (29) in a form similar to the Schmid law:

$$\tau^s = \frac{3U_{cr}}{T} - \frac{3}{T}\boldsymbol{\sigma}^{hyd} \cdot \boldsymbol{\varepsilon}^{pt,\varepsilon}. \tag{30}$$

In Eq. (30) the right-hand side can be interpreted as the slip resistance consisting of two terms: a constant term $\frac{3U_{cr}}{T}$ and a stress dependent term $\frac{3}{T}\boldsymbol{\sigma}^{hyd} \cdot \boldsymbol{\varepsilon}^{pt,\varepsilon}$. In the model we use $\frac{3U_{cr}}{T}$ as the fitting parameter corresponding to an initial value of slip resistance. After each deformation step, we correct the slip resistance with $\frac{3}{T}\boldsymbol{\sigma}^{hyd} \cdot \boldsymbol{\varepsilon}^{pt,\varepsilon}$, until at least one slip system is active. After activation of slip systems, we allow for the strain hardening to take place. For strain hardening of the phase, we use the dislocation density-based hardening law provided in appendix A.

While models combining the stress-assisted and strain-induced transformations can be formulated within a continuum thermodynamic principle framework (Levitas et al., 2017a; Ma and Hartmaier, 2015), more physical approaches dealing with dislocations face issues in attempting to unify the kinetics laws. While growth of preexisting phases can be unified, the physics of nucleation cannot, since the physics of nucleation is fundamentally different in stress-assisted versus in strain-induced transformations. In particular, the strain-induced transformation requires consideration of dislocations dissociating. In summary, the nucleation related to formation of twins and ε-martensite would be the main challenge to unification.

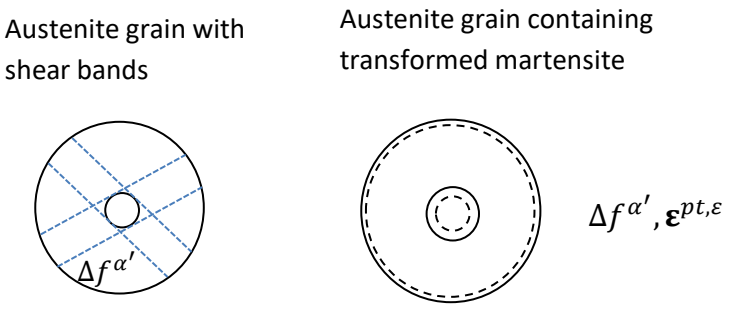

Figure 2. Schematic showing an austenite grain represented with a sphere before and after martensitic transformation of volume $\Delta f^{\alpha'}$.

3. Results

In order to simulate mechanical response, evolution of texture, and evolution of phases using EPSC, the model is initialized with a starting texture for *γ*-austenite, initial grain shapes, a set of single crystal elastic constants per phase, and a set of slip systems per phase. In addition, parameters pertaining to the hardening law and the kinetic models are calibrated and validated by comparing the simulated and measured data in terms of mechanical response, texture, and phase fractions. The model is used to interpret the data of an austenitic steel.

For the present simulation cases, the initial texture is assumed to be random with each grain initialized to be a spherical inclusion into the effective medium. Both texture and grain shape evolve with deformation and transformation. Simple tension (ST), simple compression (SC), and torsion boundary conditions are imposed and these cases simulated to certain strain levels. The ST/SC are simulated by imposing normal strain increments along the loading direction, while enforcing zero normal stresses in the lateral directions and zero shear strains. Torsion is simulated with plane stress state in the plane containing 1 and 2 directions, while applying shear strain increments, $\Delta\varepsilon_{12}$, and setting the normal strains in directions 1 and 2 to zero (Jahedi et al., 2015a; Jahedi et al., 2015b; Knezevic et al., 2013b; Zecevic et al., 2015b, c).

The experimental results for austenitic steel 18Cr-10Ni reported in (Lebedev and Kosarchuk, 2000) have been simulated by the developed model. Chemical composition of this austenitic steel is provided in table 2. The material was tested in ST, SC, and torsion at 77 K and 293 K. The transformation to ε-martensite and α'-martensite happened at 77 K, while at 293 K there was no appreciable transformation. The determination of material parameters involves hardening parameters controlling the mechanical response and kinetic laws parameters controlling the onset and rate of transformation. In our first attempt to simulate the data, only the strain-induced kinetics model was active as is meant to be appropriate for the studied austenitic steel (Olson and Cohen, 1982). The model calibration involves adjusting three sets of parameters i.e. a set of the hardening law parameters for austenite, a set of the hardening law parameters for martensite, and a set of the kinetics law parameters. The measured mechanical response

is a homogenized response of martensite and austenite, while the latter is transforming into the former. Arriving at a unique set of hardening parameters for both phases and the transformation kinetics simultaneously would be challenging since similar effects on the stress strain curve can be achieved by changing parameters of either martensite or austenite. To remove such ambiguities in the fitting procedure, we adjust the hardening parameters for austenite at 293 K, where the mechanical response is solely governed by the austenite phase with no phase transformation happening (see Fig. 3a). The hardening law is temperature sensitive and we allow this intrinsic temperature sensitivity to predict the response of austenite at 77 K. The kinetic law parameters were calibrated using the tension data at 77 K, see Fig. 3b and c. The α'-martensite hardening law parameters were calibrated by comparing the measured and simulated stress-strain curve for tension at 77 K, see Fig. 3a. The parameters are provided in tables 3 and 4. The single crystal elastic constants for austenite are $C_{11} = 209\ GPa$, $C_{12} = 133\ GPa$ and $C_{44} = 121\ GPa$. The single crystal elastic constants for α'-martensite are $C_{11} = 234\ GPa$, $C_{12} = 135\ GPa$ and $C_{44} = 118\ GPa$ (Wang et al., 2016). The crystal elastic constants for ε-martensite are calculated based on formulations from (Fellinger et al., 2019; Pronk and Frenkel, 2003) and are $C_{11} = 268.7\ GPa$, $C_{12} = 128.6\ GPa$, $C_{13} = 77.67\ GPa$, $C_{33} = 319.7\ GPa$ and $C_{44} = 49.26\ GPa$. The $\{1\bar{1}1\}\langle 110\rangle$ and the $\{110\}\langle 1\bar{1}1\rangle$ slip systems are used for austenite and α'-martensite, respectively, while slip systems in the HCP phase of ε-martensite are restricted to pyramidal slip on $\{01\bar{1}1\}_\varepsilon$ planes in $\langle 5\bar{1}\bar{4}\bar{3}\rangle_\varepsilon$ and $\langle 0\bar{1}12\rangle_\varepsilon$ directions, with the restrictions $\langle 5\bar{1}\bar{4}\bar{3}\rangle_\varepsilon \cdot [0001] < 0$ and $\langle 0\bar{1}12\rangle_\varepsilon \cdot [0001] > 0$, facilitating $\varepsilon \rightarrow \alpha'$ transformation. The specific slip systems have been listed in table 1. The simulated volume fractions of ε-martensite and α'-martensite for torsion and compression, shown in Fig. 3b and c, respectively, are predictions. To further demonstrate predictive characteristics and flexibility of the developed model, Fig. 4 presents results of simulations performed after enabling a small amount of the stress-assisted transformation, in addition to the already active strain-induced kinetics law. As is evident, the small addition of stress-assisted transformation improves the predictions. Simultaneous occurrence of strain-induced and stress-assisted transformations has been observed experimentally (Maxwell et al., 1974; Snell et al., 1977). Figure 5 shows the predicted texture evolution per phase for the three simulation cases. These predictions have been validated using the model presented in (Zecevic et al., 2019) and since essentially indistinguishable, they are not shown. Additionally, texture evolution after the small addition of stress-assisted transformation is not appreciably different and these pole figures are not shown.

It should be noted that some of the parameters pertaining to the hardening and kinetics laws such as slip resistance, drag stress, and SFE can be calculated using first principle- or atomistic-based simulation tools instead of calibrated using experimental data. Several recent works involving a continuum/atomistic approach to predicting stress-state sensitive phase transformations and in particular the role of instabilities in addition to the free energy minima have attempted to do so (Chen et al., 2019; Levitas et al., 2017a, b; Zarkevich et al., 2018). However some difficulties in attempting to perform such calculations for ESPC would likely arise due to complex chemical compositions of the technologically relevant austenitic steels used in the present work. Moreover, considering that some of the parameters like the initial hardening slope, k_1, are volume averaged values, some form of averaging of the first principles calculations would be necessary to facilitate meaningful extractions and/or comparisons. Nevertheless, having the parameters either calculated using the first principle calculations or measured, as parameters

like slip resistance and SFE are measureable quantities, would eliminate any non-uniqueness, since obtaining good fits of experimental does not usually warrant that sets of parameters are unique.

Table 2. Chemical composition (wt. %) of the austenitic steel considered in the present study. Fe balances the provided composition.

C	Cr	Ni	Si	Mo	Mn	Cu	Ti	V
0.07	15.4	12.3	0.43	1.91	1.45	0.12	0.41	0.05

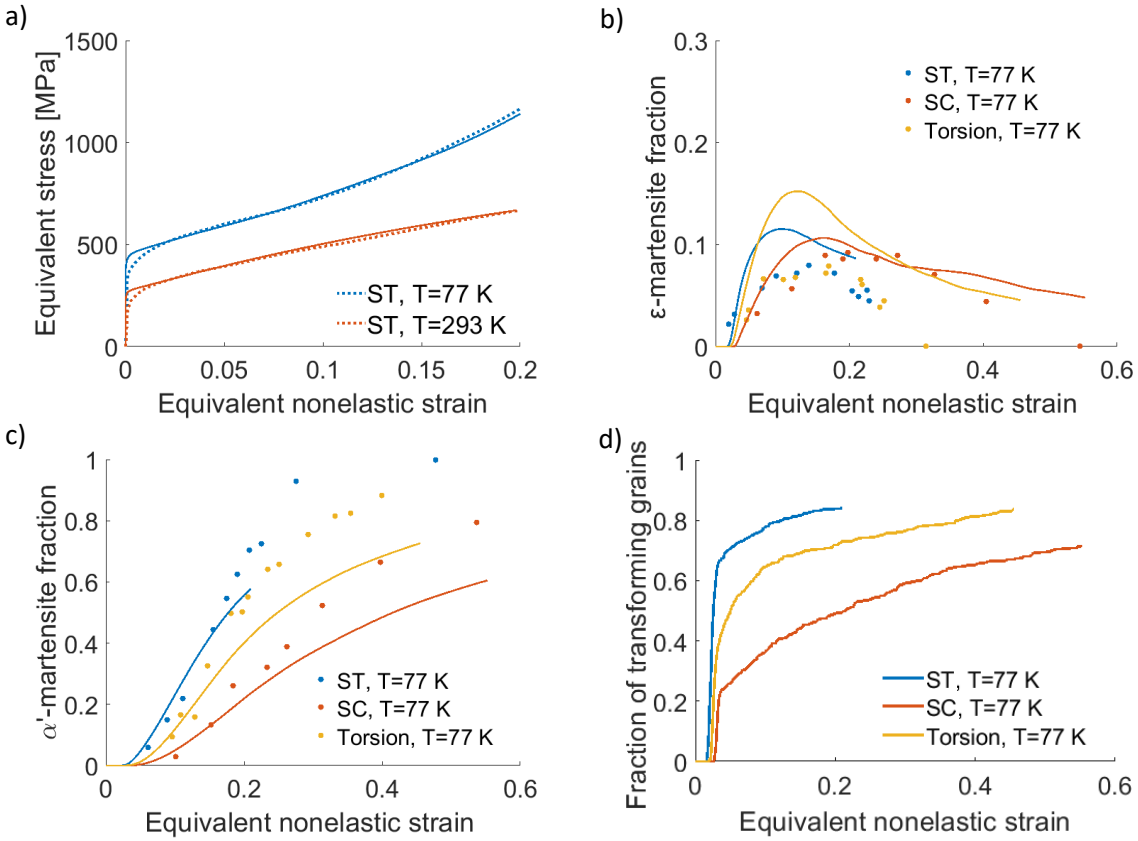

Figure 3. Comparison between measured and predicted (a) stress-strain response for simple tension (ST) at 77 K and 293 K, (b) volume fraction of ε-martensite for simple tension (ST) to 0.2 strain, simple compression (SC) to 0.55 strain, and torsion to 0.4 shear strain at 77 K, (c) volume fraction of α'-martensite for ST, SC, and torsion at 77 K, and (d) fraction of austenite grains that transform for 18Cr-10Ni austenitic steel. Dots are experimental data, while solid lines are simulation results with only strain-induced phase transformations enabled in the model.

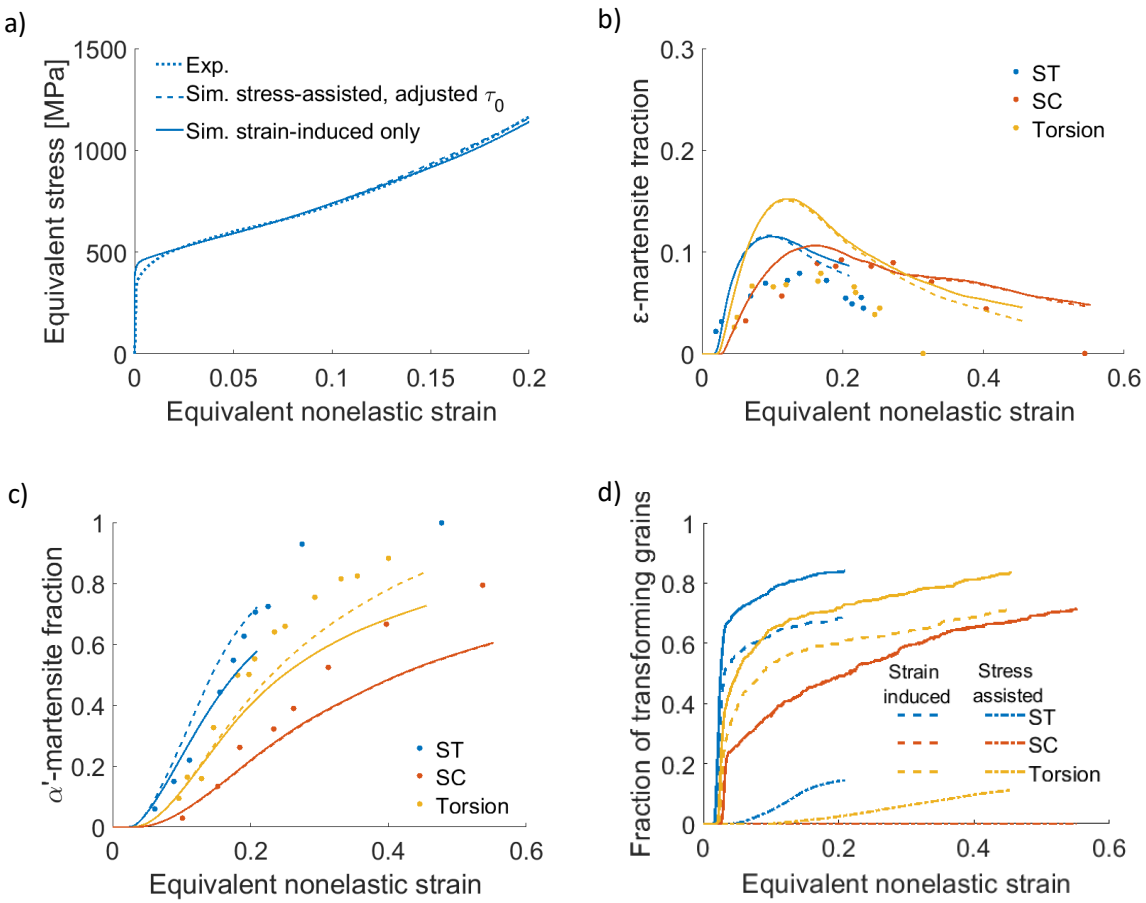

Figure 4. Comparison between measured and predicted (a) stress-strain response for ST at T = 77 K, (b) volume fraction of ε-martensite for ST, SC, and torsion at 77 K, (c) volume fraction of α'-martensite for ST, SC, and torsion at 77 K, (d) fraction of austenite grains that transformed for 18Cr-10Ni austenitic steel. Dots are experimental data, solid lines are simulation results with only strain-induced phase transformations enabled, and dashed lines (and dash-dotted lines in d) are simulation results with both the stress-assisted and strain-induces transformations enabled.

a) γ-austenite simulated in tension

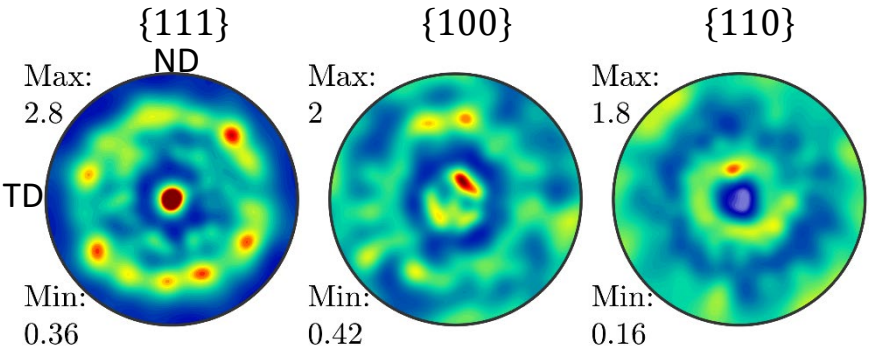

α'-martensite simulated in tension

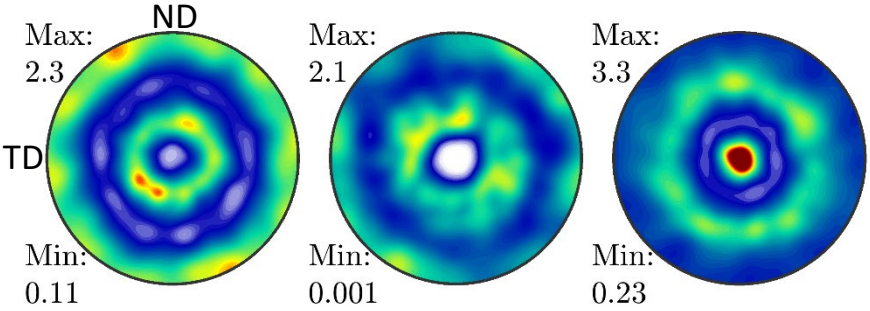

b) γ-austenite simulated in compression

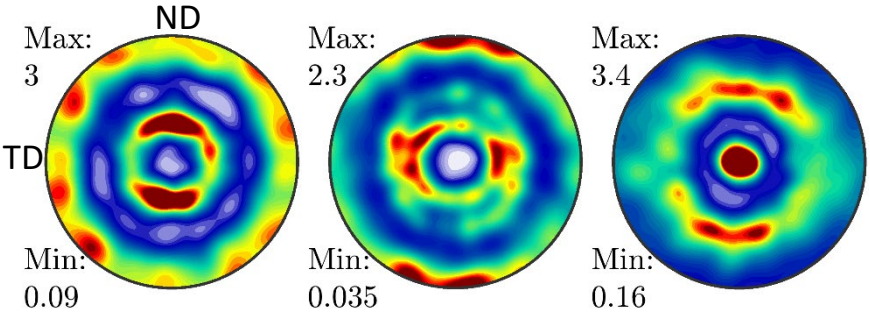

α'-martensite simulated in compression

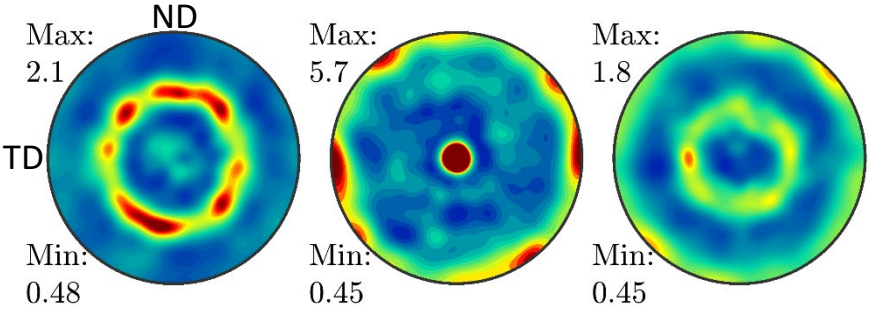

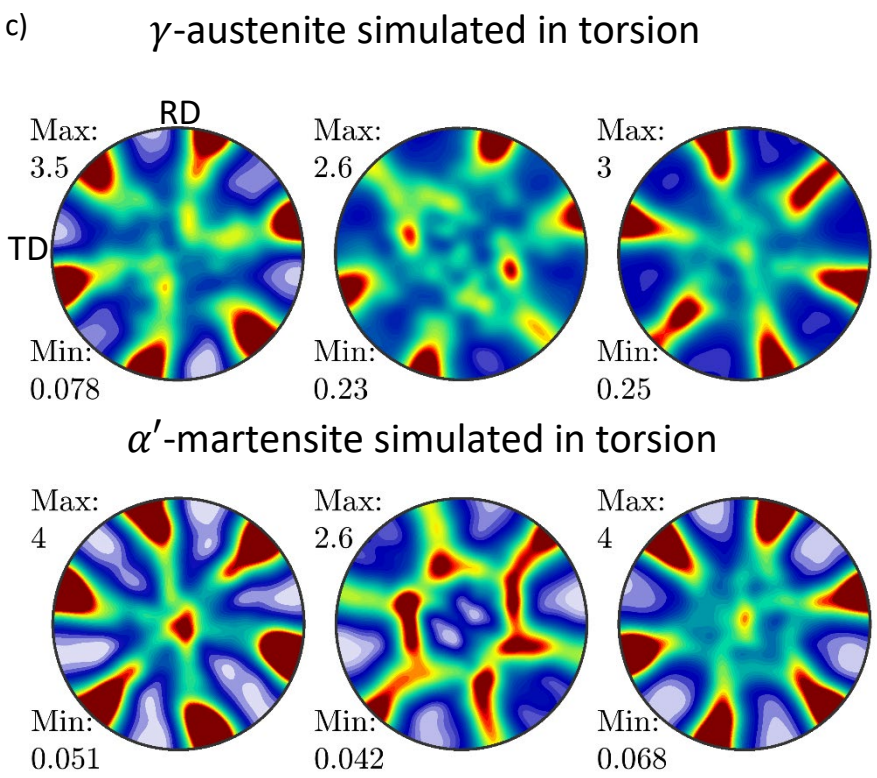

Figure 5. Pole figures showing the simulated texture evolution with strain-induced transformation only (a) ST, (b) SC, and (c) torsion to strain levels of 0.2, 0.55, and 0.4 respectively at 77 K for γ-austenite and α′-martensite. The loading direction (RD) is at the center of pole figures for ST and SC. The torsion pole figures are plotted in the shear plane.

Table 3. Parameters pertaining to the phase transformation kinetics laws.

$U_c\ [\frac{MJ}{m^3}]$	$\frac{\gamma_N}{N}\ [\frac{mJ}{m^2}]$	$f_{cr}^{\alpha'}$	f_{cr}^{ε}
65.0	7.6	0.01	0.01

Table 4. Parameters pertaining to the hardening law.

Phase	$\tau_0\ [MPa]$	$k_1\ [m^{-1}]$	g	$D\ [MPa]$	q	$\hat{b}$ [Å]
γ	$145@77K$ $80@293K$	0.92×10^{-8}	0.15	100	4	2.54
ε	100	0.21×10^{-8}	1×10^{6}*	100	4	1.47
α'	250**	1.00×10^{-8}	0.25	100	4	2.49

α'_{SA}	225	1.00×10^{-8}	0.25	100	4	2.49

* The value is high to promote linear hardening, since plastic deformation in ε transforms it into the α'-martensite. The c/a ratio is 1.58 for the HCP phase.
**The value is reduced to 225 for the simulation cases when both stress-assisted and strain-induced transformations are active.

4. Discussion

This paper developed physically based kinetics laws for both stress-assisted and strain-induced γ-austenite to α'-martensite transformation sensitive to strain path in crystal plasticity. The volume fraction evolution of martensite are predicted by the model. In terms of non-elastic equivalent strain, $\gamma \rightarrow \varepsilon$ transformation during tension starts first, followed by torsion and finally compression. The total fraction of austenite grains that form ε-martensite phase is shown in Fig 3d. The interaction of the stress state with separation between partials on active slip systems, defined by crystal orientation, determines if the grain will form ε-martensite (Zecevic et al., 2019). The process of separation between partials is the most favorable in ST, while the least favorable in SC. After initial increase of ε-martensite fraction at roughly constant rate, the $\varepsilon \rightarrow \alpha'$ transformation initiates, decreasing the rate of ε-martensite fraction evolution. At an instant, the rate of $\varepsilon \rightarrow \alpha'$ transformation is equal to $\gamma \rightarrow \varepsilon$ transformation, which is seen as the maximum in ε-martensite volume fraction. After this point, the volume fraction of ε-martensite is decreasing, meaning that the rate of $\varepsilon \rightarrow \alpha'$ transformation is greater than the rate of $\gamma \rightarrow \varepsilon$ transformation.

In the model of the strain-induced transformation developed here, the α'-martensite is the product of ε-martensite phase. The difference in content of α'-martensite between tension, torsion and compression in the model, seen in Fig 3c, is driven by the difference in ε-martensite content and behavior of ε-martensite under different stress states. The ε-martensite deforms by plastic slip accompanied by the transformation to α'-martensite. The stress state will affect the slip resistance according to Eq. (30). The slip resistance for ε-martensite is lowest for tension ($\boldsymbol{\sigma}^{hyd} \cdot \boldsymbol{\varepsilon}^{pt} > 0$), followed by torsion ($\boldsymbol{\sigma}^{hyd} \cdot \boldsymbol{\varepsilon}^{pt} = 0$) and compression ($\boldsymbol{\sigma}^{hyd} \cdot \boldsymbol{\varepsilon}^{pt} < 0$).

Note that the model under-predicts content of α'-martensite for compression and torsion. The mismatch could originate from assumption that only grains developing slip bands transform. There are experimental evidence that show even grains without slip bands form α'-martensite. The simulation cases with stress-assisted kinetics further improve the results and demonstrate flexibility of the overall model (Fig. 4). The model successfully predicts low addition of the stress-assisted transformation during SC as low magnitude of stress triaxiality inhibits the transformation (Patel and Cohen, 1953).

The kinetics models presented in this work relate the martensite fraction with the shear strain on the slip systems in each grain. The fraction of martensite depends on the crystal lattice orientation relative to the loading direction governing the stress state in the crystal. As a result, the effect of crystal lattice orientation on the fraction of martensite is intrinsically accounted for by the model. Figure 6 shows the propensity of different crystal orientations to form martensite using the inverse pole figure (IPF) maps.

Normalized values of volume fraction of ε-martensite are plotted for the strain-induced transformation under ST and SC at an arbitrary strain level during the transformation. Similarly, normalized values of driving force (Eq. 15) to obtain α'-martensite are plotted for the stress-assisted martensite transformation at an arbitrarily selected value of stress for every crystal in the IPF map. The plots for the strain-induced transformation show the transformation propensity is at the minimum for the $\langle 001 \rangle$ crystals parallel to the ST direction, while it is at the maximum for $\langle 011 \rangle$ and $\langle 111 \rangle$ crystals parallel to the ST direction. These predictions are consistent with the observations from (Burgers and Klostermann, 1965; Goodchild et al., 1970; Lagneborgj, 1964; Petit et al., 2007). In contrast, the model reveals that crystals with the <001> orientation parallel to the SC direction have the highest propensity to transform. The prediction is consistent with experimental observation reported in (Polatidis et al., 2018). The crystals compressed along <011> or <011> do not transform in SC, as reported in (Goodchild et al., 1970). Figure 6c incicates easy transformation for soft grains like those with [001] paralel with SC/ST direction (Hilkhuijsen et al., 2013).

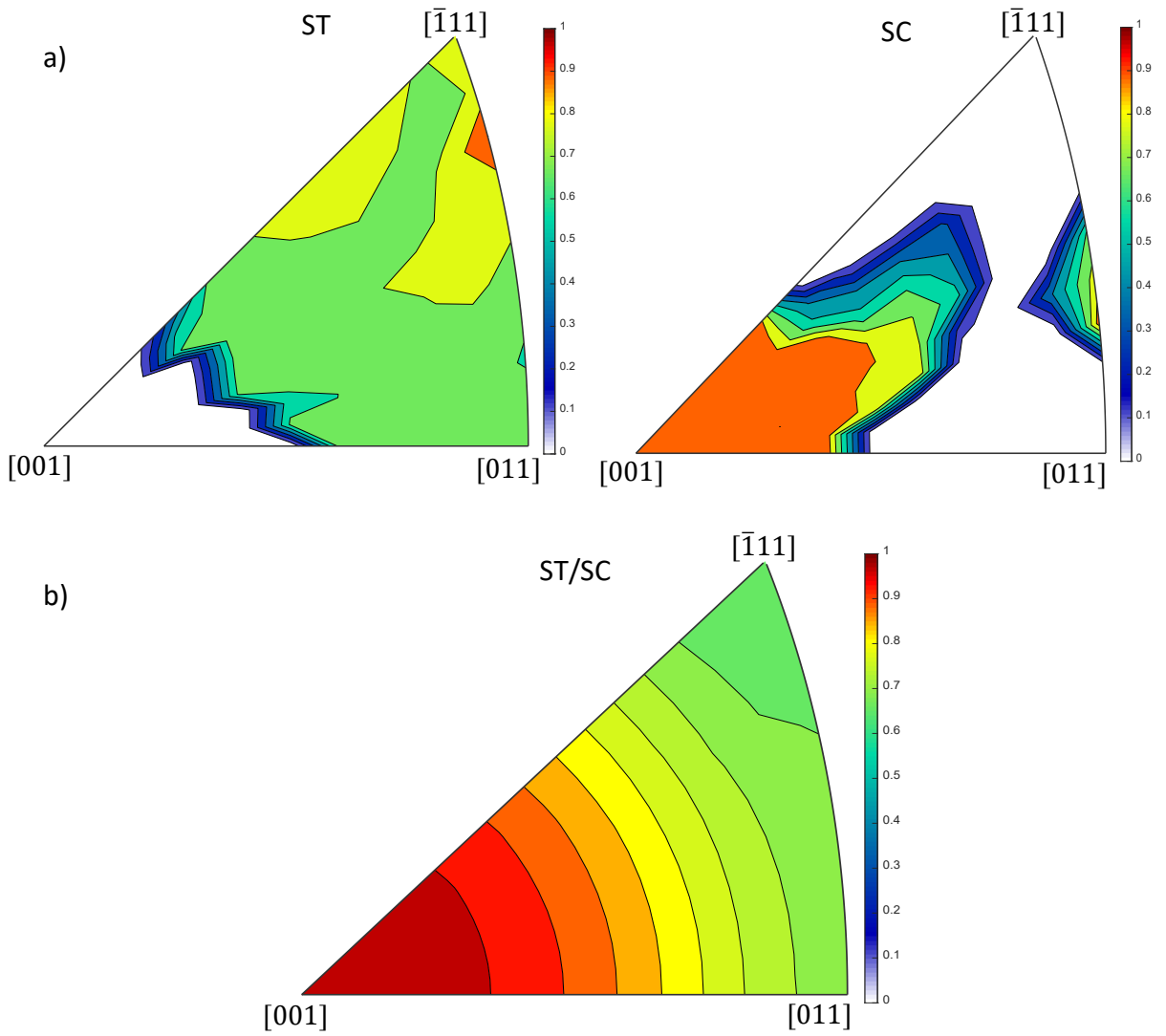

Figure 6. Contours showing the effect on crystal orientation on the probability to transform: (a) normalized volume fraction of *ε*-martensite in ST and SC and (b) normalized driving force to obtain α'-martensite in ST and SC under the stress-assisted transformation.

5. Conclusions

This paper presented kinetics models for both stress-assisted and strain-induced *γ*-austenite to *α'*-martensite transformation sensitive to strain paths. The models do not assume functions for the evolution of α'-martensite fraction and are not formulated as extensions of the empirical Olson-Cohen model but are physically based. The strain-induced transformation model conceived here treats phase transformation physically as an additional deformation mode, while the stress-assisted transformation model relies on an energy criterion. Consistent with experimental observations, the kinetics model for the strain-induced transformation is first transforming *γ*-austenite to a separate/intermediate *ε*-martensite phase in shear bands driven by local stress state sensitive motion of partial dislocations and subsequently

transforming the ε-martensite phase to α'-martensite after shear bands intersect. To model the ε-martensite morphology, a flat ellipsoid approximation is incorporated into EPSC. The stress-assisted transformation is direct from γ-austenite to α'-martensite. Crystallographic, kinetic, and thermodynamic aspects of the martensite transformation are captured by the laws. Since local crystal orientation has a strong influence on the active transformation mechanisms, the laws are implemented in EPSC. The overall implementation facilitates modeling of strain path and crystallographic texture dependence of martensitic transformation, while predicting deformation behavior of metastable austenitic steels. Simple tension, simple compression, and torsion data of an austenitic steel have been used to calibrate and to illustrate predictive characteristics of the overall implementation. In doing so, stress-strain response, phase fractions of γ-austenite, intermediate ε-martensite, and α'-martensite, and texture are all calculated, while fully accounting for the crystallography of the transformation mechanisms. Good predictions demonstrate flexibility and utility of the developed EPSC implementation.

Acknowledgments

This research was sponsored by the U.S. National Science Foundation and was accomplished under the Grant No. OIA-1757371.

Appendix A. Dislocation density-based hardening law within EPSC

The dislocation-based hardening law available in EPSC is briefly summarized for completeness of the paper. The evolution of slip resistance, within the EPSC framework, is governed by the relation:

$$\dot{\tau}_c^{c,s} = \sum_{s'} h^{ss'} \dot{\gamma}^{c,s'}, \tag{A1}$$

where $h^{ss'}$ is the hardening matrix, $\dot{\tau}_c$ is the rate of slip resistance and $\dot{\gamma}$ is the shear rate on a slip system. Assuming the slip resistance is a function of shear strain allows writing the hardening matrix as a matrix of partial derivatives:

$$h^{ss'} = \frac{\partial \tau_c^s}{\partial \gamma^{s'}}. \tag{A2}$$

Next, the evolution of slip resistance with shear strain is defined using the dislocation-based strain rate and temperature sensitive hardening law (Ardeljan and Knezevic, 2018; Ardeljan et al., 2015a; Beyerlein and Tomé, 2008 ; Knezevic et al., 2014a ; Knezevic et al., 2012 ; Knezevic et al., 2014b). α enumerates slip modes, while *s* slip systems. The total slip resistance on a slip system consists of several terms:

$$\tau_c^s = \tau_0^\alpha + \tau_{forest}^s + \tau_{debris}^\alpha, \tag{A3}$$

where τ_0^α is an initial slip resistance, τ_{forest}^s is a forest term, τ_{debris}^α is a debris term. The initial slip resistance includes all contributions to slip resistance which remain constant during deformation, e.g. the Hall-Petch contribution, the solid solution contribution etc. The forest term describes the contribution to slip resistance from the statistically stored dislocations:

$$\tau^s_{forest} = b^\alpha \chi \mu^\alpha \sqrt{\sum_{s'} L^{ss'} \rho^{s'}_{tot}} \quad \text{(A4)}$$

where b^α is the Burgers vector having values of $2.538\ 10^{-10}\ m$ and $2.488\ 10^{-10}\ m$ for austenite and martensite phases, respectively , $\chi = 0.9$ is an interaction constant, ρ^s_{tot} is the total forest dislocation density per slip system ($s \in \alpha$) and $L^{ss'}$ is a strength interaction matrix with entries set to 1 (Franciosi and Zaoui, 1982; Khadyko et al., 2016). The debris term describes the contribution to slip resistance from dislocations stored as debris (Ardeljan et al., 2017; Ardeljan et al., 2016; Ardeljan et al., 2015b):

$$\tau^\alpha_{debris} = 0.086\ \mu^\alpha b^\alpha \sqrt{\rho_{deb}}\, log\left(\frac{1}{b^\alpha \sqrt{\rho_{deb}}}\right) \quad \text{(A5)}$$

where ρ_{deb} is the debris dislocation density (Madec et al., 2003).

With known total dislocation density, $\rho^{s'}_{tot}$, and debris dislocation density, ρ_{deb}, the current value of slip resistance, τ^s_c, can be evaluated. $\rho^{s'}_{tot}$ and ρ_{deb} evolve with shear strain on the slip systems according to the evolution laws (Khadyko et al., 2016 ; Knezevic et al., 2013c; Kocks and Mecking, 1981):

$$\frac{\partial \rho^s_{tot}}{\partial \gamma^s} = k^\alpha_1 \sqrt{\sum_{s'} g^{ss'} \rho^{s'}_{tot}} - k^\alpha_2(\dot{\varepsilon}, T)\rho^{s'}_{tot}, \quad \text{(A6)}$$

where k^α_1 determines the rate of generation of statistically stored dislocations, k^α_2 is a rate-sensitive coefficient for dynamic recovery (Beyerlein and Tomé, 2008), and $g^{ss'}$ is a matrix governing the slip system interaction in terms of accumulation of forest dislocations (Khadyko et al., 2016; Kocks et al., 1991; Teodosiu and Raphanel, 1991). Here we adopted the diagonal form of $g^{ss'}$ matrix, i.e. $g^{ss} = 1$ and $g^{ss'} = 0$, meaning that there are no interactions between slip systems in terms of accumulation of forest dislocations. The initial total dislocation density is set to $10^{11}\ m^{-2}$. While k^α_1 is a constant number governing the rate of generation of dislocations, k^α_2 is defined in terms of temperature and strain rate as (Knezevic et al., 2013a; Knezevic et al., 2016; Zecevic et al., 2016a):

$$\frac{k^\alpha_2}{k^\alpha_1} = \frac{\chi b^\alpha}{g^\alpha}\left(1 - \frac{k_B T}{D^\alpha (b^\alpha)^3} ln\left(\frac{\dot{\varepsilon}}{\dot{\varepsilon}_0}\right)\right), \quad \text{(A7)}$$

where, k_B, $\dot{\varepsilon}_0 = 10^7\ s^{-1}$, g^α and D^α are the Boltzmann constant, a reference strain rate, an effective activation enthalpy and a drag stress, respectively. The debris dislocation density in the grain evolves with shear strain on the slip systems as:

$$\frac{\partial \rho_{deb}}{\partial \gamma^s} = q^\alpha b^\alpha \sqrt{\rho_{deb}}\ k^\alpha_2(\dot{\varepsilon}, T)\rho^s_{tot}, \quad \text{(A8)}$$

where q^α is a dislocation recovery rate constant. The initial debris dislocation density is 0.1 m^{-2}.

Appendix B. α'-martensite crystal orientation and phase transformation strain associated with the stress-assisted phase transformation

A new martensite grain has a specific crystallographic relationship with its parent austenite grain. The lattice parameters of austenite and martensite are 0.3589 nm and 0.2873 nm, respectively (Wang et al., 2016). From these lattice parameters, the Bain strain and stretching tensor needed for the transformation from the FCC to the BCC structure can be calculated. Enforcing the condition that a direction in the plane

(101) and the normal to the plane containing the direction $[\bar{1}01]$ are invariant after transformation, two unique solutions for the rotation matrix can be found (Bhadeshia, 2001; Malet and Godet, 2015). The two solutions produce two solutions for the transformation matrix from a parent austenite grain/frame ($\mathbf{g}^a$) to a product martensite grain/frame ($\mathbf{g}^m$). $\mathbf{g}^m$ and $\mathbf{g}^a$ describe the coordinate transformation from the local crystal lattice frame to the sample frame for a grain of martensite and austenite, respectively. The transformation matrix corresponding to the usually reported orientation relationship in experimental studies is adopted ($\mathbf{g}^m = \mathbf{g}^a(\mathbf{T}^{a\to m})^T$), where:

$$\mathbf{T}^{a\to m} = \begin{bmatrix} 0.7239 & -0.6896 & -0.0183 \\ 0.6778 & 0.7160 & -0.1670 \\ 0.1283 & 0.1085 & 0.9858 \end{bmatrix}. \quad \text{(B1)}$$

The total deformation gradient related to the phase transformation is the product of the rotation matrix and the right stretching tensor described by the Bain strain. The total deformation gradient related to shape change is found by assuming a lattice invariant deformation occurs prior to Bain stretching and rotation (Cahn et al., 1996). The lattice invariant deformation is simple shear on the $(101)_\gamma$ plane in the direction $[\bar{1}01]_\gamma$, consistent with the above adopted invariant direction and plane normal (Bhadeshia, 2001). The shape change deformation is the general plane strain on the habit plane with the plane normal $\mathbf{p} = [-0.1846,\ -0.7821,\ -0.5951]^T$ in the direction $\mathbf{d} = [0.2090,\ -0.7088, 0.6738]^T$. The deformation gradient related to the general plane strain is (Wang et al., 2016):

$$\mathbf{F}_{shape} = \begin{bmatrix} 0.9913 & -0.0369 & -0.0281 \\ 0.0296 & 1.1252 & 0.0953 \\ -0.0281 & -0.1190 & 0.9094 \end{bmatrix}. \quad \text{(B2)}$$

The phase transformation strain in the parent austenite frame is calculated from the deformation gradient describing the shape change (Wang et al., 2016):

$$\boldsymbol{\varepsilon}^{pt,\sigma} = \frac{\mathbf{F}_{shape}^T \mathbf{F}_{shape} - \mathbf{I}}{2} = \begin{bmatrix} -0.0078 & 0.0 & -0.0253 \\ 0.0 & 0.1408 & 0.0 \\ -0.0253 & 0.0 & -0.0815 \end{bmatrix} \quad \text{(B3)}$$

After applying 24 cubic crystal symmetry operators, 24 transformation matrices, $\mathbf{T}^{a\to m}$, and the phase transformation strains, $\boldsymbol{\varepsilon}^{pt,\sigma}$, are generated, corresponding to 24 marentsite variants. One out of 24, which is the most active i.e. the most energetically favorable is selected for the transformed grain.

In what follows, we elaborate more on the derivation of Eq. (18). We arrive to Eq. (18), which is suitable to implement into mean-field models such as EPSC, from a sophisticated full-field formulation for modeling phase transformations. To that end, we use a particular phase-field model from (Levin et al., 2013). A block of austenite with martensite nucleus, as a necessary condition for stress-assisted transformation, is considered with the phase-field variable of 0 in austenite and 1 in martensite. Small strains and elastic materials were assumed. The additional Ginzburg-Landau field equation for the determination of the phase-field variable is (Levin et al., 2013):

$$\frac{1}{L}\dot{\eta} = \beta\nabla^2\eta + \boldsymbol{\sigma}\cdot\boldsymbol{\varepsilon}^{pt}\frac{\partial\varphi(\eta)}{\partial\eta} - \frac{\partial\psi_{el}(\eta)}{\partial\eta} - \frac{\partial f(\eta)}{\partial\eta}, \quad \text{(B4)}$$

where L is a kinetic coefficient, η is the phase-field variable, β is a gradient energy coefficient, φ is an interpolation function, ψ_{el} is the elastic strain energy density, and f is a contribution from the free energy difference between the two phases, i.e. the chemical driving force, and a double well potential. Note that the term $\beta\nabla^2\eta$ is coming from an interface energy. In mean-field formulations, the objective is to reduce the field η to a single variable giving a fraction of martensite, $f^{\alpha'}$ in an austenite volume. After averaging of Eq. (B4) over volumes of austenite and martensite, we get:

$$\frac{1}{L}\frac{1}{V}\int_V \dot{\eta}\, dV = \frac{1}{L}\dot{f}^{\alpha'} = \frac{1}{V_{int}}\int_{V_{int}} \left(\beta\nabla^2\eta + \boldsymbol{\sigma}\cdot\boldsymbol{\varepsilon}^{pt}\frac{\partial\varphi(\eta)}{\partial\eta} - \frac{\partial\psi_{el}(\eta)}{\partial\eta} - \frac{\partial f(\eta)}{\partial\eta}\right) dV, \tag{B5}$$

where V_{int} is the volume of interface. Since in regions of uniform $\eta = 0$ and $\eta = 1$ all terms in Eq. (B4) vanish, the integration is only over the interface volume. Rewriting Eq. (B5) with volume averaged terms gives:

$$\frac{1}{L}\dot{f}^{\alpha'} = F_{int} + U - F_{el} - \Delta G_{ch}. \tag{B6}$$

Assuming uniform stress in the interface domain, which corresponds to austenite stress, we write:

$$U = \boldsymbol{\sigma}\cdot\boldsymbol{\varepsilon}^{pt}\frac{1}{V_{int}}\int_{V_{int}}\frac{\partial\varphi(\eta)}{\partial\eta}\, dV. \tag{B7}$$

Since we are not dealing with strain path reversals, we limit $\dot{f}^{\alpha'} \geq 0$. This condition implies that preexisting martensite nucleus cannot disappear i.e. any reverse transformation from martensite to austenite is not possible. From here, we see that the condition for growth of an initial nucleus is:

$$\boldsymbol{\sigma}\cdot\boldsymbol{\varepsilon}^{pt} \geq \frac{-F_{int}+F_{el}+\Delta G_{ch}}{\frac{1}{V_{int}}\int_{V_{int}}\frac{\partial\varphi(\eta)}{\partial\eta}dV}. \tag{B8}$$

Once this condition is fulfilled, the rate of martensite fraction can be found from Eq. (B6). If we set the kinetic coefficient to a large value in Eq. (B6), we end up with a condition for the calculation of $\dot{f}^{\alpha'}$ as:

$$\boldsymbol{\sigma}\cdot\boldsymbol{\varepsilon}^{pt} = \frac{-F_{int}+F_{el}+\Delta G_{ch}}{\frac{1}{V_{int}}\int_{V_{int}}\frac{\partial\varphi(\eta)}{\partial\eta}dV}. \tag{B9}$$

Since we do not know how the right hand side depends on $f^{\alpha'}$, we assume that the ratio $\frac{-F_{int}+F_{el}+\Delta G_{ch}}{\frac{1}{V_{int}}\int_{V_{int}}\frac{\partial\varphi(\eta)}{\partial\eta}dV}$ is a constant. As a result, the behavior of phase transformation process is similar to the perfectly plastic yield function behavior. Differentiating Eq. (B9) with respect to time, provides an equation for the calculation of $\dot{f}^{\alpha'}$, which is analogous to the consistency condition (Eq. 18). A similar condition to onset of transformation was implemented in a mesoscopic continuum thermomechanical approach to modeling of strain-induced martensitic transformation in (Levitas et al., 1998). As grain stress continuously evolves every increment in EPSC with the evolution of hardening and crystal reorientation, the mechanical driving force for the stress-assisted transformation calculated using Eq. (15) takes into account such changes in stress per grain. This driving force is compared with the criterion to onset of transformation. A theory of phase transformation in elastoplastic materials developed in (Levitas, 2000a, b) also takes this stress

variation into account, as well as the continuum theory of strain-induced transformation at the intersection of shear bands (Levitas et al., 1998).

A consistent relation $\frac{-F_{int}+F_{el}+\Delta G_{ch}}{\frac{1}{V_{int}}\int_{V_{int}}\frac{\partial\varphi(\eta)}{\partial\eta}dV}$ in function of $f^{\alpha'}$ could be derived by fitting to results of a full-field model, which is a significant effort and outside the scope of this work. The assumption of not considering the interfacial energy and the boundary misfit strain energy explicitly in EPSC is one of the intrinsic assumptions involved in the mean-field modeling framework. While complex stress fields in the vicinity of the phase interfaces can be captured by full-field phase transformation models, such fields reduce to uniform stress per grain in the modelling approach relying on the mean-field model such as EPSC. A new grain in the microstructure introduces a new interface i.e. a new grain boundary. However, the intrinsic feature of the mean-field models is to assume uniform stress within a crystal, disregarding any grain boundary effects. While evaluating the effects of ignoring the interfacial energy and the boundary misfit strain energy will be attempted in future works using a full-field solution procedures, we speculate that the effects would be small on the overall material response but likely more significant on the local material response. It is worth noting that modeling of deformation twinning in mean-field models involves making the same assumption as for phase transformations. Twinning models usually have an evolution law for $\frac{-F_{int}+F_{el}}{\frac{1}{V_{int}}\int_{V_{int}}\frac{\partial\varphi(\eta)}{\partial\eta}dV}$ with dislocation density build up, also known as the twin hardening law. Twins form within parent grains and are separated from the parent by parent-twin boundaries. Nevertheless, they are modeled as independent entities/grains in the mean-field models. EPSC framework considering twinning has been shown to work well in capturing overall material response in a number of studies (Agnew et al., 2006; Zecevic et al., 2015a).

Appendix C. α'-martensite crystal orientation and phase transformation strain associated with the strain-induced phase transformation

To consistently derive the crystal orientation of the martensite grains and the associated phase transformation strain, we follow the mechanisms of strain-induced transformations as described in (Bogers and Burgers, 1964; Bracke et al., 2007; Olson and Cohen, 1972). In the strain-induced transformation, martensite forms at the intersection of two shear bands. The atoms in one shear band have positions corresponding to *T*/2 shear, where *T* refers to twinning shear. The twinning shear is $T = \frac{b_p}{d_{111}} = \frac{1}{\sqrt{2}}$, (Eq. 24), where d_{111} is the spacing between the $\{111\}_\gamma$ planes. The *T*/2 shear structure can be formed from ε-martensite by shuffles on every 2nd $\{0001\}_\varepsilon$ plane for $\frac{a_\gamma}{12}\langle 1\bar{1}\bar{2}\rangle_\gamma$. The shuffle transforms the $\{01\bar{1}1\}_\varepsilon$ planes into uniformly distorted $\{111\}_\gamma$ planes. Next, the partial dislocations in austenite, averaging one on every three $\{111\}_\gamma$ planes, pass through the uniformly distorted $\{111\}_\gamma$ planes in the *T*/2 structure. These partial dislocations are part of the other shear band causing the *T*/3 shear in the *T*/2 shear band. The intersection of the *T*/2 and *T*/3 shear bands has a BCC structure. Additionally, there is a volume increase of 2.59%, determined by the lattice parameters of austenite, a_γ =0.3589 nm, and

martensite, $a_{\alpha'}$=0.2873 nm (Wang et al., 2016). The orientation relationship between austenite, ε-martensite and α'-martensite is (Bracke et al., 2007):

$$\{111\}_\gamma \parallel \{110\}_{\alpha'} \parallel \{0001\}_\varepsilon \quad \text{(C1)}$$

$$\langle 110\rangle_\gamma \parallel \langle 111\rangle_{\alpha'} \parallel \langle 2\bar{1}\bar{1}0\rangle_\varepsilon \,. \quad \text{(C2)}$$

The deformation gradient for uniform shearing in the leading partial shearing direction, $\hat{\mathbf{s}}^{l,p}$, on the $\langle 0\bar{1}1\rangle\{111\}_\gamma$ slip systems is:

$$\mathbf{F}^S = \mathbf{I} + S\hat{\mathbf{s}}^{l,p} \otimes \mathbf{n}\,, \quad \text{(C3)}$$

where *S* is the amount of shear, i.e. *T*/2 or *T*/3, in the direction $\hat{\mathbf{s}}^{l,p}$ on the plane with plane normal $\mathbf{n}$. In our implementation, we first identify two slip systems that will form *T*/2 shuffle and *T*/3 shear. In fact, the first slip system converts ε-martensite into *T*/2 structure by shuffles during the passage of the partial dislocations from the *T*/3 shear band. We remind that the ε-martensite is the one having the highest SFW. To determine the relationship between the direction of the *T*/3 shear and the shuffles to produce the *T*/2 structure from ε-martensite, we examine the tetrahedron from (Bogers and Burgers, 1964), shown in Figure C1a. The four $\{111\}$ planes shown in Figure C1a have their normals pointing outwards from the tetrahedron, as in the Thompson tetrahedron. We use the plane labels from the Thompson tetrahedron shown in Figure C1d for convenience. Note that for our choice of the plane normal, $\mathbf{n}$, the shearing direction due to the leading partial, $\hat{\mathbf{s}}^{l,p}$, is always from the Greek to the Roman letter on the Thompson tetrahedron. If partial dislocations with burgers vector in the direction δC pass on every 2nd ABC plane the ε-martensite within the first shear band is generated, shown in Figure C1b. The *T*/2 structure is formed by shuffling every 2nd ABC plane for $\frac{a_\gamma}{12}$ in δA, δB or δC directions. The structure obtained after shuffling in δA is identical to uniform shearing of the tetrahedron for *T*/2 in δA direction on ABC plane. Likewise, the structures obtained after δB and δC shuffles correspond to structures generated by uniform *T*/2 shear in δB and δC respectively. The ε configuration is labeled with ‘, while the configuration after uniform shearing for *T*/2 on ABC planes is labeled with ‘’.

We focus on plane BCD for examining the *T*/3 shear, the role of the second slip system. The indicated directions in the BCD plane for the FCC structure in Figure C1a represent the possible shearing directions due to the passage of the leading partial and are labeled as αB, αC and αD. If the *T*/3 shearing is on the BCD plane in the direction αB, the needed shuffle is in δC on every 2nd basal plane, transforming two out of the six $\{1\bar{1}01\}_\varepsilon$ planes to two uniformly distorted $\{111\}_\gamma$ planes, B’’C’’D’’ and A’’D’’C’’. This shuffle produces the *T*/2 shear transforming the HCP structure to the exact *T*/2 structure as the consequence of the shearing. After allowing the *T*/3 shear on plane B’’C’’D’’ in α''B’’, a BCC is formed, as shown in Figure C1c. Similar procedure can be performed for the *T*/3 shearing in the $\alpha''C''$ direction, resulting in shuffle in $\delta''A''$ direction and the formation of the BCC structure of different orientation, both respecting the relationships described with relations (C1) and (C2). However, it is not possible to choose a shuffle that would lead to the BCC structure after shearing in $\alpha''D''$. While choosing the *T*/3 shear plane and direction, we disregard the slip systems which have the geometrical relationship between the leading partial shear and the *T*/2 shear plane analogous to the relation between the αD direction and the ABC plane. From the

remaining active planes in FCC, we choose the plane with the highest RSS on the leading partial to be the *T*/3 plane. If there are no active planes which satisfy these conditions, the search is expanded to include all slip planes in a crystal. Once we have determined the *T*/3 and *T*/2 planes and the directions, we can define the martensite orientation.

The atomic illustrations in Figure C1 are created from an atomic model developed to explore the criteria of forming the BCC structure. The main criterion is that the second partial shear must be on an HCP slip plane that is parallel to a $\{111\}_\gamma$ plane and in the direction of the shear band. The combinations of planes referenced in (Bracke et al., 2007; Olson and Cohen, 1972; Yang et al., 2014) produce near-cubic shapes with 90±5° angles. Therefore, an additional criterion is the final shape must have angles within 5° from orthogonal. Table C1 lists the combinations of shears that successfully produce the BCC structure and satisfy the two criteria. The model reveals the only valid combinations to involve pyramidal slips, which agrees with experimental observations. The model also predicts the second partial shear to be reversible where both positive and negative directions produce valid BCC structure. However, this is not allowed in the code since the negative direction would be in the opposite direction of the shear band, which violates the selection criterion.

The deformation gradient related to the austenite to α'-martensite transformation can be written as:

$$\mathbf{F}^{pt} = \mathbf{F}^{vol}\mathbf{F}^{T/3}\mathbf{F}^{T/2}\,, \tag{C4}$$

where $\mathbf{F}^{T/2}$ is the deformation gradient describing the shearing on the *T*/2 plane and $\mathbf{F}^{T/3}$ is the deformation gradient describing the shearing on the *T*/3 plane both calculated using Eq. (C3), while $\mathbf{F}^{vol}$ is the deformation gradient describing the volume change, defined as the volumetric part of the Bain deformation gradient (Eq. (B2)). The volume fraction of shear bands is calculated from plastic strain with Eq. (22). Therefore, at any instant in simulation plastic strain contains $\mathbf{F}^{T/2}$ and $\mathbf{F}^{T/3}$ deformation. Since the shear part of the phase transformation is already accounted for by the plastic strain, the phase transformation strain is simply calculated as:

$$\boldsymbol{\varepsilon}^{pt,\varepsilon} = \frac{\left(\mathbf{F}^{vol}\right)^T\mathbf{F}^{vol} - \mathbf{I}}{2}\,. \tag{C5}$$

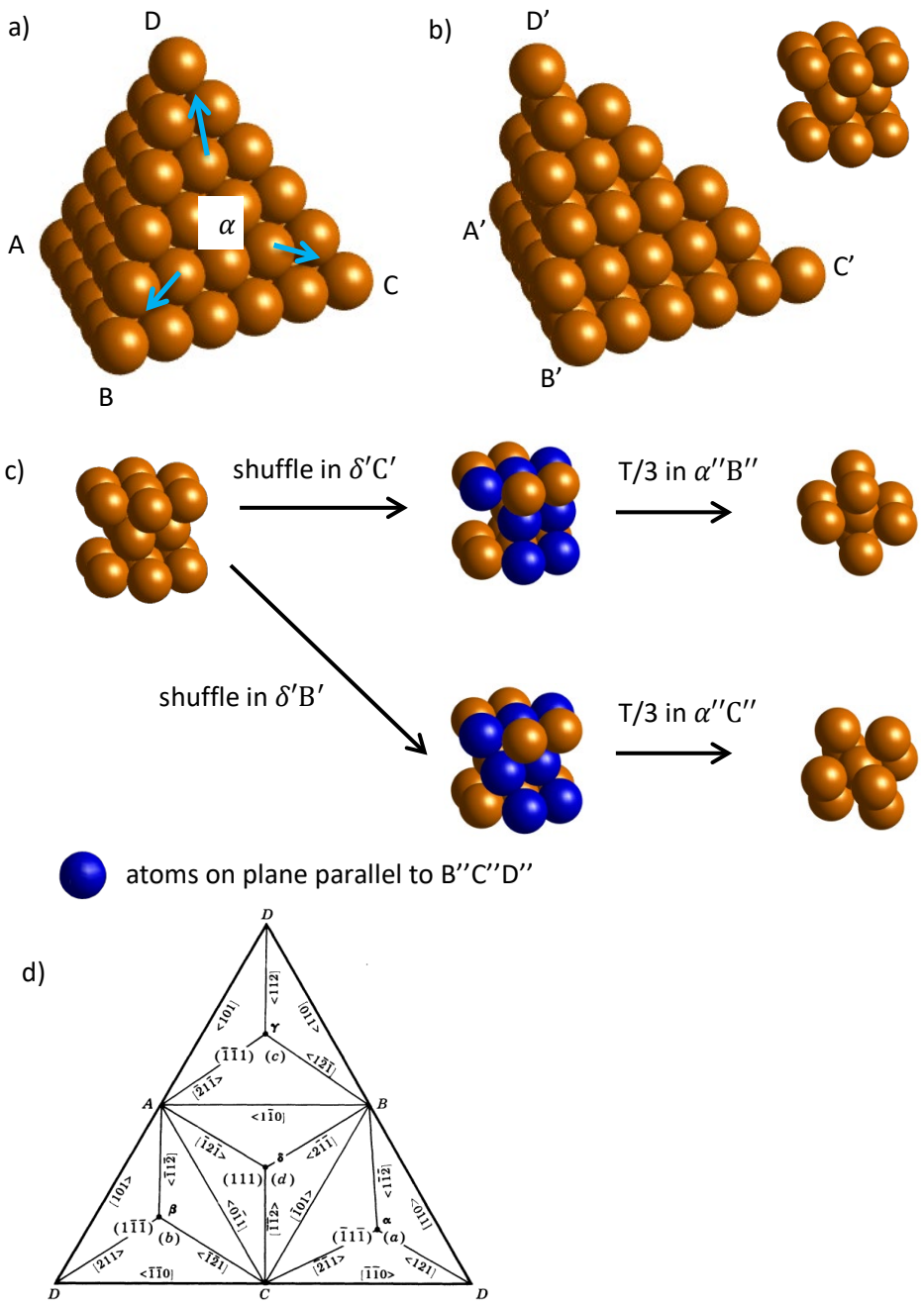

Figure C1. (a) Tetrahedron consisting of the four $\{111\}$ planes in the FCC austenite (Bogers and Burgers, 1964). (b) Tetrahedron after passage of partial dislocations on every 2nd ABC plane with the Burgers vector determined from the Thompson tetrahedron along with the resulting HCP unit cell. (c) Transformation of an HCP $\{1\bar{1}01\}_{\varepsilon}$ plane to uniformly distorted BCD plane, followed by shearing for *T*/3 in two different directions to produce BCC crystal structure. (d) Thompson tetrahedron (Cahn et al., 1996). The indicated directions in the BCD plane in (a) represent the possible shearing directions due to the passage of the leading partial and are labeled as αB, αC and αD.

Table C1. Combinations of partial, shuffle ($T/2$), and shear ($T/3$) directions that produce BCC α'-martensite. After examining in detail the combinations of $T/2$ shear and $T/3$ shear in the FCC Thompson Tetrahedron, four possible outcomes after $T/2$ shear are found: (1) The structure's HCP slip planes are not parallel to a $\{111\}$ plane on the tetrahedron, therefore no possible $T/3$ shear can be applied. These cells are colored red. (2) The combination does not form a $T/2$ structure. These cells are left white. (3) The general structure after $T/3$ shear is body-centered, but the unit cell is sheared to deviate from tetragonal definition. These cells are colored gray. (4) The T/3 shear successfully produces a BCC structure with angles within 5° difference from orthogonal. These cells are colored blue.

First partial→	δC					
$T/3\downarrow$ $T/2\rightarrow$	$\delta' A'$	$A'\delta'$	$\delta' B'$	$B'\delta'$	$\delta' C'$	$C'\delta'$
$ABC-\delta'' A''$						
$ABC-A''\delta''$						
$ABC-\delta'' B''$						
$ABC-B''\delta''$						
$ABC-\delta'' C''$						
$ABC-C''\delta''$						
$BCD-\alpha'' B''$						
$BCD-B''\alpha''$						
$BCD-\alpha'' C''$						
$BCD-C''\alpha''$						
$BCD-\alpha'' D''$						
$BCD-D''\alpha''$						
$ACD-\beta'' A''$						
$ACD-A''\beta''$						
$ACD-\beta'' C''$						
$ACD-C''\beta''$						
$ACD-\beta'' D''$						
$ACD-D''\beta''$						
$ABD-\gamma'' A''$						
$ABD-A''\gamma''$						
$ABD-\gamma'' B''$						
$ABD-B''\gamma''$						
$ABD-\gamma'' D''$						
$ABD-D''\gamma''$						

References

Agnew, S.R., Brown, D.W., Tomé, C.N., 2006. Validating a polycrystal model for the elastoplastic response of magnesium alloy AZ31 using in situ neutron diffraction. Acta. Mater. 54, 4841-4852.

Ardeljan, M., Beyerlein, I.J., Knezevic, M., 2017. Effect of dislocation density-twin interactions on twin growth in AZ31 as revealed by explicit crystal plasticity finite element modeling. Int. J. Plast. 99, 81-101.

Ardeljan, M., Beyerlein, I.J., McWilliams, B.A., Knezevic, M., 2016. Strain rate and temperature sensitive multi-level crystal plasticity model for large plastic deformation behavior: Application to AZ31 magnesium alloy. Int. J. Plast. 83, 90-109.

Ardeljan, M., Knezevic, M., 2018. Explicit modeling of double twinning in AZ31 using crystal plasticity finite elements for predicting the mechanical fields for twin variant selection and fracture analyses. Acta. Mater. 157, 339-354.

Ardeljan, M., Knezevic, M., Nizolek, T., Beyerlein, I.J., Mara, N.A., Pollock, T.M., 2015a. A study of microstructure-driven strain localizations in two-phase polycrystalline HCP/BCC composites using a multi-scale model. Int. J. Plast. 74, 35-57.

Ardeljan, M., McCabe, R.J., Beyerlein, I.J., Knezevic, M., 2015b. Explicit incorporation of deformation twins into crystal plasticity finite element models. Computer Methods in Applied Mechanics and Engineering 295, 396-413.

Barrett, T.J., Knezevic, M., 2019. Deep drawing simulations using the finite element method embedding a multi-level crystal plasticity constitutive law: Experimental verification and sensitivity analysis. Computer Methods in Applied Mechanics and Engineering 354, 245-270.

Beese, A.M., Mohr, D., 2011. Effect of stress triaxiality and Lode angle on the kinetics of strain-induced austenite-to-martensite transformation. Acta Materialia 59, 2589-2600.

Beyerlein, I.J., Tomé, C.N., 2008. A dislocation-based constitutive law for pure Zr including temperature effects. Int. J. Plast. 24, 867-895.

Bhadeshia, H.K.D.H., 2001. Worked examples in the Geometry of Crystals. The Institute of Metals North American Publications Center.

Bhattacharyya, A., Weng, G.J., 1994. An energy criterion for the stress-induced martensitic transformation in a ductile system. Journal of the Mechanics and Physics of Solids 42, 1699-1724.

Bogers, A.J., Burgers, W.G., 1964. Partial dislocations on the {110} planes in the B.C.C. lattice and the transition of the F.C.C. into the B.C.C. lattice. Acta Metallurgica 12, 255-261.

Bracke, L., Kestens, L., Penning, J., 2007. Transformation mechanism of α′-martensite in an austenitic Fe–Mn–C–N alloy. Scripta Materialia 57, 385-388.

Burgers, W.G., Klostermann, J.A., 1965. Influence of the direction of deformation on the transition of austenite into martensite. Acta Metallurgica 13, 568-572.

Byun, T.S., 2003. On the stress dependence of partial dislocation separation and deformation microstructure in austenitic stainless steels. Acta Materialia 51, 3063-3071.

Cahn, R.W., Haasen, P., Haasen, P., 1996. Physical Metallurgy, 4 ed. Elsevier Science.

Cantara, A.M., Zecevic, M., Eghtesad, A., Poulin, C.M., Knezevic, M., 2019. Predicting elastic anisotropy of dual-phase steels based on crystal mechanics and microstructure. International Journal of Mechanical Sciences 151, 639-649.

Chen, H., Levitas, V.I., Xiong, L., 2019. Amorphization induced by 60° shuffle dislocation pileup against different grain boundaries in silicon bicrystal under shear. Acta. Mater. 179, 287-295.

Christian, J.W., Mahajan, S., 1995. Deformation twinning. Prog. Mater. Sci. 39, 1-157.

Copley, S.M., Kear, B.H., 1968. The dependence of the width of a dissociated dislocation on dislocation velocity. Acta Metallurgica 16, 227-231.

Das, Y.B., Forsey, A.N., Simm, T.H., Perkins, K.M., Fitzpatrick, M.E., Gungor, S., Moat, R.J., 2016. In situ observation of strain and phase transformation in plastically deformed 301 austenitic stainless steel. Materials & Design 112, 107-116.

Fellinger, M.R., Hector Jr, L.G., Trinkle, D.R., 2019. Impact of solutes on the lattice parameters and elastic stiffness coefficients of hcp Fe from first-principles calculations. Comput. Mater. Sci. 164, 116-126.

Franciosi, P., Zaoui, A., 1982. Multislip in f.c.c. crystals a theoretical approach compared with experimental data. Acta Metallurgica 30, 1627-1637.

Ghorbanpour, S., Alam, M.E., Ferreri, N.C., Kumar, A., McWilliams, B.A., Vogel, S.C., Bicknell, J., Beyerlein, I.J., Knezevic, M., 2020. Experimental characterization and crystal plasticity modeling of anisotropy, tension-compression asymmetry, and texture evolution of additively manufactured Inconel 718 at room and elevated temperatures. Int. J. Plast. 125, 63-79.

Ghorbanpour, S., Zecevic, M., Kumar, A., Jahedi, M., Bicknell, J., Jorgensen, L., Beyerlein, I.J., Knezevic, M., 2017. A crystal plasticity model incorporating the effects of precipitates in superalloys: Application to tensile, compressive, and cyclic deformation of Inconel 718. Int. J. Plast. 99, 162-185.

Goodchild, D., Roberts, W.T., Wilson, D.V., 1970. Plastic deformation and phase transformation in textured austenitic stainless steel. Acta Metallurgica 18, 1137-1145.

Haidemenopoulos, G.N., Aravas, N., Bellas, I., 2014. Kinetics of strain-induced transformation of dispersed austenite in low-alloy TRIP steels. Materials Science and Engineering: A 615, 416-423.

Han, H.N., Lee, C.G., Oh, C.-S., Lee, T.-H., Kim, S.-J., 2004. A model for deformation behavior and mechanically induced martensitic transformation of metastable austenitic steel. Acta Materialia 52, 5203-5214.

Hecker, S.S., Stout, M.G., Staudhammer, K.P., Smith, J.L., 1982. Effects of Strain State and Strain Rate on Deformation-Induced Transformation in 304 Stainless Steel: Part I. Magnetic Measurements and Mechanical Behavior. Metallurgical Transactions A 13, 619-626.

Hilkhuijsen, P., Geijselaers, H.J., Bor, T.C., 2013. The influence of austenite texture on the martensitic transformation of an austenitic stainless steel. J. Alloys Compd. 577S, S609-S613.

Huang, J.H., Liu, H.-K., 1998. ON A FLAT ELLIPSOIDAL INCLUSION OR CRACK IN THREE-DIMENSIONAL ANISOTROPIC MEDIA. International Journal of Engineering Science 36, 143-155.

Iwamoto, T., Tsuta, T., Tomita, Y., 1998. Investigation on deformation mode dependence of strain-induced martensitic transformation in trip steels and modelling of transformation kinetics. International Journal of Mechanical Sciences 40, 173-182.

Jahedi, M., Ardeljan, M., Beyerlein, I.J., Paydar, M.H., Knezevic, M., 2015a. Enhancement of orientation gradients during simple shear deformation by application of simple compression. J. Appl. Phys. 117, 214309.

Jahedi, M., Knezevic, M., Paydar, M., 2015b. High-Pressure Double Torsion as a Severe Plastic Deformation Process: Experimental Procedure and Finite Element Modeling. J. Mater. Eng. Perform. 24, 1471-1482.

Khadyko, M., Dumoulin, S., Cailletaud, G., Hopperstad, O.S., 2016. Latent hardening and plastic anisotropy evolution in AA6060 aluminium alloy. Int. J. Plast. 76, 51-74.

Kim, H., Lee, J., Barlat, F., Kim, D., Lee, M.-G., 2015. Experiment and modeling to investigate the effect of stress state, strain and temperature on martensitic phase transformation in TRIP-assisted steel. Acta Materialia 97, 435-444.

Knezevic, M., Beyerlein, I.J., Brown, D.W., Sisneros, T.A., Tomé, C.N., 2013a. A polycrystal plasticity model for predicting mechanical response and texture evolution during strain-path changes: Application to beryllium. Int. J. Plast. 49, 185-198.

Knezevic, M., Beyerlein, I.J., Lovato, M.L., Tomé, C.N., Richards, A.W., McCabe, R.J., 2014a. A strain-rate and temperature dependent constitutive model for BCC metals incorporating non-Schmid effects: Application to tantalum–tungsten alloys. International Journal of Plasticity 62, 93-104.

Knezevic, M., Capolungo, L., Tomé, C.N., Lebensohn, R.A., Alexander, D.J., Mihaila, B., McCabe, R.J., 2012. Anisotropic stress-strain response and microstructure evolution of textured α-uranium. Acta. Mater. 60, 702-715.

Knezevic, M., McCabe, R.J., Lebensohn, R.A., Tomé, C.N., Liu, C., Lovato, M.L., Mihaila, B., 2013b. Integration of self-consistent polycrystal plasticity with dislocation density based hardening laws within an implicit finite element framework: Application to low-symmetry metals. J. Mech. Phys. Solids 61, 2034-2046.

Knezevic, M., McCabe, R.J., Tomé, C.N., Lebensohn, R.A., Chen, S.R., Cady, C.M., Gray Iii, G.T., Mihaila, B., 2013c. Modeling mechanical response and texture evolution of α-uranium as a function of strain rate and temperature using polycrystal plasticity. Int. J. Plast. 43, 70-84.

Knezevic, M., Nizolek, T., Ardeljan, M., Beyerlein, I.J., Mara, N.A., Pollock, T.M., 2014b. Texture evolution in two-phase Zr/Nb lamellar composites during accumulative roll bonding. Int. J. Plast. 57, 16-28.

Knezevic, M., Zecevic, M., Beyerlein, I.J., Lebensohn, R.A., 2016. A numerical procedure enabling accurate descriptions of strain rate-sensitive flow of polycrystals within crystal visco-plasticity theory. Computer Methods in Applied Mechanics and Engineering 308, 468-482.

Kocks, U.F., Franciosi, P., Kawai, M., 1991. A Forest Model of Latent Hardening and its Application to Polycrystal Deformations. Textures and Microstructures 14, 1103-1114.

Kocks, U.F., Mecking, H., 1981. Kinetics of Flow and Strain-Hardening. Acta Metall. 29, 1865-1875.

Lagneborgj, R., 1964. The martensite transformation in 18% Cr-8% Ni steels. Acta Metall. 12, 823-843.

Lebedev, A.A., Kosarchuk, V.V., 2000. Influence of phase transformations on the mechanical properties of austenitic stainless steels. International Journal of Plasticity 16, 749-767.

Lebensohn, R., Solas, D., Canova, G., Brechet, Y., 1996. Modelling damage of Al □ Zn □ Mg alloys. Acta Materialia 44, 315-325.

Lentz, M., Klaus, M., Beyerlein, I.J., Zecevic, M., Reimers, W., Knezevic, M., 2015a. In situ X-ray diffraction and crystal plasticity modeling of the deformation behavior of extruded Mg–Li–(Al) alloys: An uncommon tension–compression asymmetry. Acta. Mater. 86, 254-268.

Lentz, M., Klaus, M., Wagner, M., Fahrenson, C., Beyerlein, I.J., Zecevic, M., Reimers, W., Knezevic, M., 2015b. Effect of age hardening on the deformation behavior of an Mg–Y–Nd alloy: In-situ X-ray diffraction and crystal plasticity modeling. Mater. Sci. Eng. A 628, 396-409.

Levin, V.A., Levitas, V.I., Zingerman, K.M., Freiman, E.I., 2013. Phase-field simulation of stress-induced martensitic phase transformations at large strains. International Journal of Solids and Structures 50, 2914-2928.

Levitas, V.I., 2000a. Structural changes without stable intermediate state in inelastic material. Part I. General thermomechanical and kinetic approaches. Int. J. Plast. 16, 805-849.

Levitas, V.I., 2000b. Structural changes without stable intermediate state in inelastic material. Part II. Applications to displacive and diffusional–displacive phase transformations, strain-induced chemical reactions and ductile fracture. Int. J. Plast. 16, 851-892.

Levitas, V.I., Chen, H., Xiong, L., 2017a. Lattice instability during phase transformations under multiaxial stress: Modified transformation work criterion. Physical Review B 96, 054118.

Levitas, V.I., Chen, H., Xiong, L., 2017b. Triaxial-Stress-Induced Homogeneous Hysteresis-Free First-Order Phase Transformations with Stable Intermediate Phases. Physical Review Letters 118, 025701.

Levitas, V.I., Idesman, A.V., Olson, G.B., 1998. Continuum modeling of strain-induced martensitic transformation at shear-band intersections. Acta. Mater. 47, 219-233.

Ma, A., Hartmaier, A., 2015. A study of deformation and phase transformation coupling for TRIP-assisted steels. Int. J. Plast. 64, 40-55.

Madec, R., Devincre, B., Kubin, L., Hoc, T., Rodney, D., 2003. The role of collinear interaction in dislocation-induced hardening. Science 301, 1879-1882.

Malet, L., Godet, S., 2015. On the relation between orientation relationships predicted by the phenomenological theory and internal twins in plate martensite. Scripta Materialia 102, 83-86.
Mansourinejad, M., Ketabchi, M., 2017. Modification of Olson–Cohen model for predicting stress-state dependency of martensitic transformation. Materials Science and Technology 33, 1948-1954.
Marketz, F., Fischer, F., 1994. Micromechanical modelling of stress-assisted martensitic transformation. Modelling and Simulation in Materials Science and Engineering 2, 1017-1046.
Martin, S., Ullrich, C., Rafaja, D., 2015. Deformation of Austenitic CrMnNi TRIP/TWIP Steels: Nature and Role of the ε−martensite. Materials Today: Proceedings 2, S643-S646.
Masson, R., Bornert, M., Suquet, P., Zaoui, A., 2000. An affine formulation for the prediction of the effective properties of nonlinear composites and polycrystals. Journal of the Mechanics and Physics of Solids 48, 1203-1227.
Maxwell, P.C., Goldberg, A., Shyne, J.C., 1974. Stress-Assisted and strain-induced martensites in FE-NI-C alloys. Metallurgical Transactions 5, 1305-1318.
McCabe, R.J., Beyerlein, I.J., Carpenter, J.S., Mara, N.A., 2014. The critical role of grain orientation and applied stress in nanoscale twinning. Nature Communications 5, 3806.
Miller, M.P., McDowell, D.L., 1996. The Effect of Stress-State on the Large Strain Inelastic Deformation Behavior of 304L Stainless Steel. Journal of Engineering Materials and Technology 118, 28-36.
Neil, C.J., Wollmershauser, J.A., Clausen, B., Tomé, C.N., Agnew, S.R., 2010. Modeling lattice strain evolution at finite strains and experimental verification for copper and stainless steel using in situ neutron diffraction. Int. J. Plast. 26, 1772-1791.
Olson, G., Cohen, M., 1982. Stress-assisted isothermal martensitic transformation: application to TRIP steels. MTA 13, 1907-1914.
Olson, G.B., 2002. Effects of Stress and Deformation on Martensitic Formation, in: Aaronson, H. (Ed.), Encyclopedia of Materials. Elsevier.
Olson, G.B., Azrin, M., 1978. Transformation behavior of TRIP steels. Metallurgical Transactions A 9, 713-721.
Olson, G.B., Cohen, M., 1972. A mechanism for the strain-induced nucleation of martensitic transformations. Journal of the Less Common Metals 28, 107-118.
Olson, G.B., Cohen, M., 1975. Kinetics of strain-induced martensitic nucleation. Metallurgical Transactions A 6, 791.
Olson, G.B., Cohen, M., 1976. A general mechanism of martensitic nucleation: Part I. General concepts and the FCC → HCP transformation. Metallurgical Transactions A 7, 1897-1904.
Patel, J., Cohen, M., 1953. Criterion for the action of applied stress in the martensitic transformation. Acta Metall. 1, 531-538.
Petit, B., Gey, N., Cherkaoui, M., Bolle, B., Humbert, M., 2007. Deformation behavior and microstructure/texture evolution of an annealed 304 AISI stainless steel sheet. Experimental and micromechanical modeling. International Journal of Plasticity 23, 323-341.
Polatidis, E., Hsu, W.N., Šmíd, M., Panzner, T., Chakrabarty, S., Pant, P., Van Swygenhoven, H., 2018. Suppressed martensitic transformation under biaxial loading in low stacking fault energy metastable austenitic steels. Scr. Mater. 147, 27-32.
Poulin, C.M., Barrett, T.J., Knezevic, M., 2020a. Inferring Post-Necking Strain Hardening Behavior of Sheets by a Combination of Continuous Bending Under Tension Testing and Finite Element Modeling. Experimental Mechanics 60, 459-473.
Poulin, C.M., Korkolis, Y.P., Kinsey, B.L., Knezevic, M., 2019. Over five-times improved elongation-to-fracture of dual-phase 1180 steel by continuous-bending-under-tension. Mater. Des. 161, 95-105.
Poulin, C.M., Vogel, S.C., Korkolis, Y.P., Kinsey, B.L., Knezevic, M., 2020b. Experimental studies into the role of cyclic bending during stretching of dual-phase steel sheets. International Journal of Material Forming https://doi.org/10.1007/s12289-019-01530-2

Pronk, S., Frenkel, D., 2003. Large difference in the elastic properties of fcc and hcp hard-sphere crystals. Physical review letters 90, 255501.

Risse, M., Lentz, M., Fahrenson, C., Reimers, W., Knezevic, M., Beyerlein, I.J., 2017. Elevated Temperature Effects on the Plastic Anisotropy of an Extruded Mg-4 Wt Pct Li Alloy: Experiments and Polycrystal Modeling. Metall. Mater. Trans. A 48, 446-458.

Santacreu, P., Glez, J.C., Chinouilh, G., Froehlich, T., 2006. Behaviour model of austenitic stainless steels for automotive structural parts.

Shen, Y.F., Li, X.X., Sun, X., Wang, Y.D., Zuo, L., 2012. Twinning and martensite in a 304 austenitic stainless steel. Materials Science and Engineering: A 552, 514-522.

Snell, E.O., Shyne, J.C., Goldberg, A., 1977. Stress-assisted and strain-induced martensite morphologies in an Fe-21Ni-0.6C alloy. Metallography 10, 299-314.

Stringfellow, R.G., Parks, D.M., Olson, G.B., 1992. A constitutive model for transformation plasticity accompanying strain-induced martensitic transformations in metastable austenitic steels. Acta Metallurgica et Materialia 40, 1703-1716.

Talonen, J., Hänninen, H., 2007. Formation of shear bands and strain-induced martensite during plastic deformation of metastable austenitic stainless steels. Acta Materialia 55, 6108-6118.

Talyan, V., Wagoner, R.H., Lee, J.K., 1998. Formability of stainless steel. Metallurgical and Materials Transactions A 29, 2161-2172.

Teodosiu, C., Raphanel, J.L., 1991. Finite element simulations of large elastoplastic deformations of multicrystals. Proceedings of the International Seminar MECAMAT91, 153-168.

Tian, Y., Gorbatov, O.I., Borgenstam, A., Ruban, A.V., Hedström, P., 2017. Deformation Microstructure and Deformation-Induced Martensite in Austenitic Fe-Cr-Ni Alloys Depending on Stacking Fault Energy. Metall. Mater. Trans. A 48, 1-7.

Turner, P.A., Tomé, C.N., 1994. A study of residual stresses in Zircaloy-2 with rod texture. Acta Metall. Mater. 42, 4143-4153.

Ullrich, C., Eckner, R., Krüger, L., Martin, S., Klemm, V., Rafaja, D., 2016. Interplay of microstructure defects in austenitic steel with medium stacking fault energy. Materials Science and Engineering: A 649, 390-399.

Wang, H., Jeong, Y., Clausen, B., Liu, Y., McCabe, R.J., Barlat, F., Tomé, C.N., 2016. Effect of martensitic phase transformation on the behavior of 304 austenitic stainless steel under tension. Materials Science and Engineering: A 649, 174-183.

Yang, X.-S., Sun, S., Wu, X.-L., Ma, E., Zhang, T.-Y., 2014. Dissecting the Mechanism of Martensitic Transformation via Atomic-Scale Observations. Scientific Reports 4, 6141.

Yang, X.-S., Sun, S., Zhang, T.-Y., 2015. The mechanism of bcc α' nucleation in single hcp ε laths in the fcc $\gamma \rightarrow$ hcp $\varepsilon \rightarrow$ bcc α' martensitic phase transformation. Acta Materialia 95, 264-273.

Yukio, K., 1987. Kinetics of deformation-induced transformation of dispersed austenite in two alloy systems. Massachusetts Institute of Technology.

Zarkevich, N.A., Chen, H., Levitas, V.I., Johnson, D.D., 2018. Lattice instability during solid-solid structural transformations under a general applied stress tensor: Example of Si I$\rightarrow$ Si II with metallization. Physical review letters 121, 165701.

Zecevic, M., Beyerlein, I.J., Knezevic, M., 2017. Coupling elasto-plastic self-consistent crystal plasticity and implicit finite elements: Applications to compression, cyclic tension-compression, and bending to large strains. Int. J. Plast. 93, 187-211.

Zecevic, M., Beyerlein, I.J., McCabe, R.J., McWilliams, B.A., Knezevic, M., 2016a. Transitioning rate sensitivities across multiple length scales: Microstructure-property relationships in the Taylor cylinder impact test on zirconium. Int. J. Plast. 84, 138-159.

Zecevic, M., Knezevic, M., 2015. A dislocation density based elasto-plastic self-consistent model for the prediction of cyclic deformation: Application to Al6022-T4. Int. J. Plast. 72, 200-217.

Zecevic, M., Knezevic, M., 2017. Modeling of Sheet Metal Forming Based on Implicit Embedding of the Elasto-Plastic Self-Consistent Formulation in Shell Elements: Application to Cup Drawing of AA6022-T4. JOM 69, 922-929.

Zecevic, M., Knezevic, M., 2018. Latent hardening within the elasto-plastic self-consistent polycrystal homogenization to enable the prediction of anisotropy of AA6022-T4 sheets. Int. J. Plast. 105, 141-163.

Zecevic, M., Knezevic, M., 2019. An implicit formulation of the elasto-plastic self-consistent polycrystal plasticity model and its implementation in implicit finite elements. Mechanics of Materials 136, 103065.

Zecevic, M., Knezevic, M., Beyerlein, I.J., Tomé, C.N., 2015a. An elasto-plastic self-consistent model with hardening based on dislocation density, twinning and de-twinning: Application to strain path changes in HCP metals. Mater. Sci. Eng. A 638, 262-274.

Zecevic, M., Korkolis, Y.P., Kuwabara, T., Knezevic, M., 2016b. Dual-phase steel sheets under cyclic tension–compression to large strains: Experiments and crystal plasticity modeling. J. Mech. Phys. Solids 96, 65-87.

Zecevic, M., McCabe, R.J., Knezevic, M., 2015b. A new implementation of the spectral crystal plasticity framework in implicit finite elements. Mechanics of Materials 84, 114-126.

Zecevic, M., McCabe, R.J., Knezevic, M., 2015c. Spectral database solutions to elasto-viscoplasticity within finite elements: Application to a cobalt-based FCC superalloy. Int. J. Plast. 70, 151-165.

Zecevic, M., Upadhyay, M.V., Polatidis, E., Panzner, T., Van Swygenhoven, H., Knezevic, M., 2019. A crystallographic extension to the Olson-Cohen model for predicting strain path dependence of martensitic transformation. Acta. Mater. 166, 386-401.